

## Parameterization of Cloud Microphysics Based on the Prediction of Bulk Ice Particle Properties. Part II: Case Study Comparisons with Observations and Other Schemes

HUGH MORRISON

*National Center for Atmospheric Research,\* Boulder, Colorado*

JASON A. MILBRANDT

*Atmospheric Numerical Prediction Research, Environment Canada, Dorval, Quebec, Canada*

GEORGE H. BRYAN, KYOKO IKEDA, SARAH A. TESSENDORF, AND GREGORY THOMPSON

*National Center for Atmospheric Research,\* Boulder, Colorado*

(Manuscript received 20 March 2014, in final form 3 August 2014)

### ABSTRACT

A new microphysics scheme has been developed based on the prediction of bulk particle properties for a single ice-phase category, in contrast to the traditional approach of separating ice into various predefined species (e.g., cloud ice, snow, and graupel). In this paper, the new predicted particle properties (P3) scheme, described in Part I of this series, is tested in three-dimensional simulations using the Weather Research and Forecasting (WRF) Model for two contrasting well-observed cases: a midlatitude squall line and winter orographic precipitation. Results are also compared with simulations using other schemes in WRF. Simulations with P3 can produce a wide variety of particle characteristics despite having only one free ice-phase category. For the squall line, it produces dense, fast-falling, hail-like ice near convective updraft cores and lower-density, slower-falling ice elsewhere. Sensitivity tests show that this is critical for simulating high precipitation rates observed along the leading edge of the storm. In contrast, schemes that represent rimed ice as graupel, with lower fall speeds than hail, produce lower peak precipitation rates and wider, less distinct, and less realistic regions of high convective reflectivity. For the orographic precipitation case, P3 produces areas of relatively fast-falling ice with characteristics of rimed snow and low- to medium-density graupel on the windward slope. This leads to less precipitation on leeward slopes and more on windward slopes compared to the other schemes that produce large amounts of snow relative to graupel (with generally the opposite for schemes with significant graupel relative to snow). Overall, the new scheme produces reasonable results for a reduced computational cost.

### 1. Introduction

With recent increases in computer power, numerical weather prediction (NWP) using nonhydrostatic models at “convection permitting” scales (horizontal grid spacing  $\Delta x$  of a few kilometers) is now routine at many research and operational centers (e.g., Kain et al. 2008;

Lean et al. 2008; Weisman et al. 2008; Clark et al. 2012). Climate modeling is also now performed at these scales, using global “cloud resolving” models (CRMs) (e.g., Miura et al. 2007) or by embedding CRMs in each grid cell of traditional general circulation models (i.e., “super-parameterization”) (e.g., Grabowski 2001; Khairoutdinov and Randall 2001; Tao et al. 2009). The representation of microphysics is especially important in these high-resolution models because it controls distributions of latent heating and cooling and condensate loading that are directly coupled with the buoyancy and model dynamics. This is reflected by studies showing considerable sensitivity of high-resolution NWP forecasts to the use of different microphysics schemes (e.g., Colle et al. 2005; Van Weverberg et al. 2011; Clark et al. 2012; Molthan

\* The National Center for Atmospheric Research is sponsored by the National Science Foundation.

Corresponding author address: Hugh Morrison, National Center for Atmospheric Research, 3090 Center Green Drive, Boulder, CO 80301.  
E-mail: morrison@ucar.edu

and Colle 2012; Cintineo et al. 2014). Parameterizing microphysics remains challenging because of fundamental uncertainty in the underlying microphysical processes, especially for ice, the need for a reasonable level of simplicity to make schemes computationally feasible, and the inability of models to resolve small-scale cloud processes that drive the microphysics (even when using  $\Delta x \sim 1$  km).

A new bulk scheme has been developed that employs a conceptually different approach for parameterizing ice microphysics compared to existing schemes (Morrison and Milbrandt 2014, hereafter Part I). In the scheme, ice evolves in time and space through the prediction of various bulk particle properties of a single ice-phase category rather than separating ice into different predefined categories (cloud ice, snow, graupel, hail, etc.) as is traditionally done. The new scheme—referred to as the predicted particle properties (P3) scheme—includes four prognostic ice mixing ratio variables: the total ice mass, the rime ice mass, the rime volume, and the total number, allowing 4 degrees of freedom for representing the particle properties. Thus, it predicts several important physical properties (e.g., mean density, size, and rime mass fraction) as they evolve from microphysical processes including vapor deposition, riming, aggregation, and wet growth. As discussed in Part I, this approach has several conceptual advantages over the traditional approach. It allows smooth transition of particle properties based on the growth history and avoids unphysical conversion processes and thresholds and discrete transitions between predefined ice-phase categories. All parameters and processes are calculated self-consistently from mass-size and projected area-size relationships that depend on the predicted particle properties. It also represents a simplification since there are fewer prognostic variables compared to traditional schemes, reducing the computational cost.

In Part I, the overall behavior of the new scheme was illustrated using idealized two-dimensional (2D) squall-line simulations. It is also critical to test the scheme in a less idealized setting. In this paper, the scheme's practical performance is evaluated by comparing three-dimensional (3D) simulations with observations and results using other microphysics schemes. Using the Weather Research and Forecasting (WRF) Model with  $\Delta x$  of 1 and 3 km, respectively, two contrasting observationally based case studies are examined: 1) a mid-latitude squall line and 2) an extratropical cyclone with precipitation enhanced by orographic forcing. These cases were chosen since they represent distinctly different meteorological regimes yet are both important for high-impact weather. Moreover, both regimes have proven challenging to model in previous work, in part

owing to parameterization of microphysics (e.g., McCumber et al. 1991; Colle et al. 2005; Milbrandt et al. 2008; Lin and Colle 2011; Van Weverberg et al. 2012; Morrison et al. 2012). The goal of this study is to evaluate the practical performance of the new scheme relative to other schemes in WRF that employ the traditional approach for parameterizing ice microphysics. Results are analyzed in detail for both cases to explain reasons for differences among simulations. The focus of the intercomparison is on key high-resolution NWP forecast quantities: precipitation, reflectivity, and storm structure, as well as computational cost.

The paper is organized as follows. Section 2 describes the case studies and observations. An overview of the model setup is given in section 3. Section 4 provides results for the squall-line case study. Section 5 gives results for the orographic precipitation case. Summary and conclusions are provided in section 6.

## 2. Case descriptions and observations

### a. Midlatitude squall line

A large mesoscale convective system (MCS) formed in the central Great Plains of the United States after the merging of three separate convective systems that initiated during the afternoon of 19 June 2007. Early on this day, an isolated storm cell moved southward near the Kansas–Colorado border toward Oklahoma and merged with two semistationary storms that formed in the late afternoon in northern Oklahoma and far northwestern Texas. These storms evolved into a classical squall line with strong leading-edge convection and trailing stratiform precipitation. The squall line subsequently passed over central Oklahoma and was observed by dual-polarization S-band Weather Surveillance Radar-1988 Doppler (WSR-88D) at Norman, Oklahoma (KOUN) (Fig. 1). The reflectivity structure at other times (not shown) during passage of the storm over central Oklahoma was similar to that shown in Fig. 1 (Morrison et al. 2012).

This storm was the focus of several previous studies. Lang et al. (2010) investigated electrical aspects of the storm. Morrison et al. (2012) and Lebo and Morrison (2014) used this case as the basis for studies testing sensitivity to microphysics schemes and aerosol effects on storms, respectively. It was also the focus of a model intercomparison study as part of the 2012 Eighth International Cloud Modeling Workshop (Muhlbauer et al. 2013).

Measurements used as part of this study to compare with the simulations were made by the KOUN radar and two 2D video disdrometers (2DVDs; Kruger and

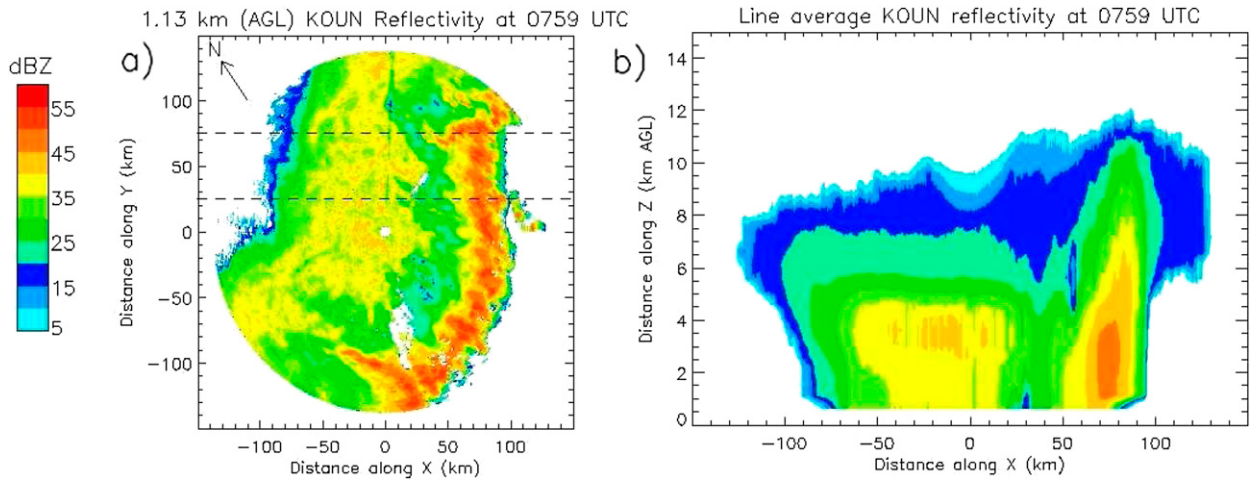


FIG. 1. Observed (a) horizontal and (b) line-averaged vertical cross sections of gridded reflectivity from KOUN for the squall-line case. The dashed lines in (a) indicate the region over which line averaging was performed for the vertical cross sections. North is indicated in the horizontal cross sections for reference since they are displayed using the rotated Cartesian grid domain.

Krajewski 2002). The two 2DVDs were deployed within the KOUN radar domain approximately 80 km apart. These measurements were used to obtain drop size distribution (DSD) parameters for comparison with the model. A more detailed description of the methodology for processing and analyzing these measurements is provided in the appendix of Morrison et al. (2012).

#### b. Extratropical cyclone–orographic forcing

This event was driven by a large extratropical cyclone and frontal system that moved through the Pacific Northwest region of the United States on 13–14 December 2001 (Garvert et al. 2005a). Strong southwesterly flow impinged on the higher terrain of the Cascade mountain range and generated significant vertical motion and enhancement of precipitation on the windward slopes of the Coastal and Cascade Ranges. This case was the focus of intensive observations collected over the central Oregon Cascades during the Improvement of Microphysical Parameterization through Observational Verification Experiment (IMPROVE)-2 field experiment (Stoelinga et al. 2003). It was one of the cases examined during the 2004 Sixth International Cloud Modeling Workshop (Grabowski 2006) and also the subject of several papers in a special section of the *Journal of the Atmospheric Sciences* (2005, Vol. 62, No. 10). Modeling studies that have examined microphysical and dynamical aspects include Garvert et al. (2005a,b), Colle et al. (2005), Garvert et al. (2007), Milbrandt et al. (2008, 2010), and Lin and Colle (2011).

Observations used for this study include microphysical measurements taken on the P-3 (not to be confused with the P3 scheme) and Convair aircraft, enhanced

soundings upstream of the Cascade Range, the WSR-88D at Portland, Oregon (KRTX), and National Center for Atmospheric Research (NCAR) S-Band dual-polarization Doppler (S-Pol) radar at Sweet Home, Oregon. Surface precipitation measurements were made from hourly cooperative observer and snow telemetry (SNOWTELE) sites across southern Washington and Oregon as well as gauges installed by the University of Washington in the IMPROVE-2 focus area specifically for this project [see Fig. 18 in Stoelinga et al. (2003)]. Further details of the measurements and analysis techniques are provided in Stoelinga et al. (2003) and Garvert et al. (2005a) and references therein.

### 3. Model description and setup

This study employs the Advanced Research Weather Research and Forecasting (WRF) Model, version 3.4.1 (Skamarock et al. 2008). WRF is a nonhydrostatic, compressible atmospheric model. The governing equations are solved using a time-split integration with third-order Runge–Kutta scheme. Horizontal and vertical advection are calculated using fifth- and third-order discretization schemes, respectively, with modifications to ensure monotonicity (Wang et al. 2009). Other aspects of the model setup pertaining to each case are described later in this section.

Simulations using the P3 scheme are compared with those using several other microphysics schemes in WRF. These include the Morrison scheme assuming either graupel or hail for the rimed-ice species (MOR-G, MOR-H), Milbrandt–Yau (MY2), National Oceanic and Atmospheric Administration (NOAA)/National

Severe Storms Laboratory (NSSL), Stony Brook University-Lin (SBU-LIN), Thompson (THO), WRF single-moment 6-class microphysics scheme (WSM6) and WRF double-moment 6-class microphysics scheme (WDM6). Each scheme is described briefly in the [appendix](#). Except for P3, all the schemes used in this study were directly from WRF, version 3.4.1, modified only for the specified droplet number or cloud condensation nuclei concentration in all schemes and a fix to the rain evaporation in NSSL. Radar reflectivity is calculated assuming Rayleigh scattering following the approach of [Smith \(1984\)](#), using the specified or predicted size distribution and particle-density parameters consistent with each scheme. There is some uncertainty because of the choice of dielectric factor and non-Rayleigh scattering [see [Smith \(1984\)](#) and Ryzkov et al. (2011) for discussion]. Particles are assumed to be composed of either liquid or ice for the calculations so that the bright band is neglected. For simplicity, the cloud droplet number concentration is set to  $250 \text{ cm}^{-3}$  in the schemes that specify this quantity (MOR-G, MOR-H, THO, P3, SBU-LIN); in NSSL, the ratio of the cloud droplet number concentration and air density is set to  $250 \times 10^6 \text{ kg}^{-1}$ . Cloud condensation nuclei concentrations are set to  $250 \text{ cm}^{-3}$  for the schemes that predict droplet concentration (MY2, WDM6).

#### a. Model setup for the squall line

WRF is used in a 3D, quasi-idealized framework to simulate the 19–20 June 2007 Oklahoma squall line. We follow the model setup specified for case 2 of the Eighth International Cloud Modeling Workshop ([Muhlbauer et al. 2013](#)), which differs somewhat from the setup of this case in [Morrison et al. \(2012\)](#). The initial sounding was generated from the 0000 UTC sounding from Lamont, Oklahoma, at low levels (pressure greater than 700 hPa) and the 0000 UTC sounding from Norman, Oklahoma, at mid- and upper levels (pressure less than or equal to 700 hPa) ([Fig. 2](#)). This was done because of possible contamination of the Lamont sounding (which was closer to the storm) from upper-level divergence and anvil cloud associated with the storm. The combined sounding was then interpolated to a vertical grid with constant 100-m spacing and smoothed with a 1–2–1 moving average. The convective available potential energy of this sounding is  $5900 \text{ J kg}^{-1}$  based on the most unstable parcel. Initial shear of the horizontal wind is specified to be zero in the direction parallel to the squall line ( $v$  wind) and  $12 \text{ m s}^{-1}$  from the surface to 5 km in the direction perpendicular to the line ( $u$  wind). This is similar to the observed value of line-normal shear based on wind profiler data from the U.S. National Oceanic and Atmospheric Administration site in Purcell,

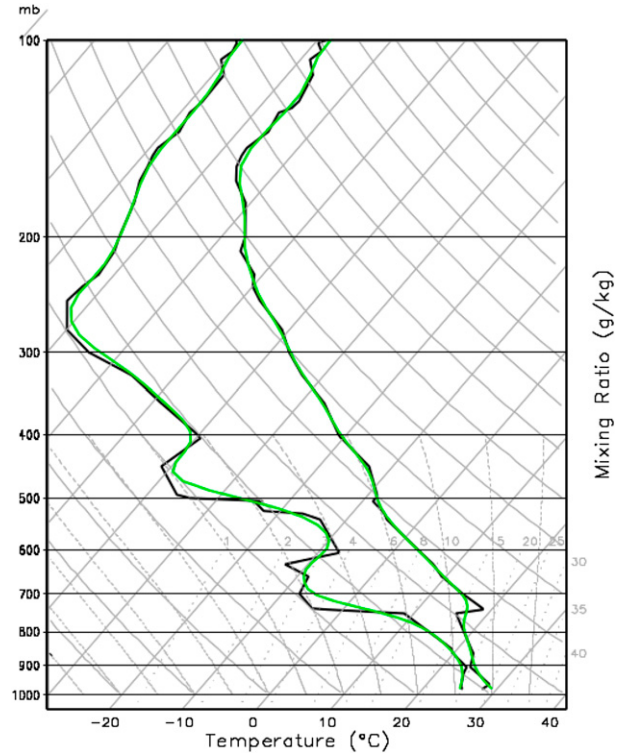


FIG. 2. Unsmoothed (black lines) and smoothed (green lines) skew- $T$  diagram for the initial environment of the squall-line case.

Oklahoma. To keep the storm within the model domain, a horizontal domain translation speed of  $17 \text{ m s}^{-1}$  was included.

The model domain is  $612 \times 122 \text{ km}^2$  with a model top at 25 km. Horizontal grid spacing is 1 km, with 100 vertical levels between the surface and top using a slight vertical grid stretching. A Rayleigh damper with damping coefficient of  $0.003 \text{ s}^{-1}$  is applied to the top 5 km. The upper and lower boundaries are free slip and rigid. Lateral boundary conditions are open in the direction perpendicular to the line and periodic along the line. Horizontal and vertical subgrid-scale mixing are calculated using a 1.5-order turbulent kinetic energy scheme ([Skamarock et al. 2008](#)). The model time step is 2.5 s.

Convection is initiated in the uniform thermodynamic environment by applying forcing to the  $u$  wind during the first hour of integration, providing convergence at low levels. The forcing term is prescribed as

$$\frac{\partial u}{\partial t} = \alpha \gamma \cos \left[ \frac{\pi(x - x_c)}{2x_r} \right] \times \left[ \cosh \left( \frac{2.5z}{z_r} \right) \right]^{-2}, \quad (1)$$

where  $x$  is distance (km) perpendicular to the line ( $x = 0 \text{ km}$  at the left domain edge),  $x_c$  is the horizontal location at the domain center,  $x_r = 10 \text{ km}$ ,  $z$  is height (km),

$z_r = 10 \text{ km}$ ,  $\alpha = 0.1 \text{ m s}^{-2}$  is the maximum forcing amplitude, and

$$\begin{aligned}\gamma &= 1 \quad t \leq 3300 \text{ s}, \\ \gamma &= 1 - (t - 3300)/300 \text{ s}, \quad 3300 \text{ s} < t < 3600 \text{ s}, \\ \gamma &= 0 \quad t \geq 3600 \text{ s},\end{aligned}\quad (2)$$

where  $t$  is time. To initiate 3D motion, random fluctuations to the initial perturbation potential temperature field are applied in a 40-km-wide region centered on the  $u$  convergence with a maximum amplitude of  $\pm 0.05 \text{ K}$ .

#### b. Model setup for the orographic precipitation case

WRF is used in a “real case” configuration to simulate the orographic precipitation case from IMPROVE-2. Initial conditions and lateral boundary forcing data are from U.S. Global Forecast System “Final” analysis. The model domain is  $1200 \times 830 \text{ km}^2$  covering a large portion of the northeastern Pacific Ocean, southwestern Canada, and the western United States. The horizontal grid spacing is 3 km. The model top is 100 hPa with 72 sigma levels over a stretched vertical grid. A Rayleigh damper with damping coefficient of  $0.03 \text{ s}^{-1}$  is applied to the upper 5 km. The model time step is 5 s. Model integrations are for 36 h from 0000 UTC 13 December to 1200 UTC 14 December.

Physical parameterizations for this case besides microphysics include radiation, planetary boundary layer/turbulent mixing (PBL), and surface processes. Shortwave and longwave radiation are calculating using the GCM version of the Rapid Radiative Transfer Model (RRTMG) (Iacono et al. 2008) with a 5-min radiation time step. The Yonsei University nonlocal PBL scheme (Hong et al. 2006) is employed. Horizontal subgrid-scale mixing is treated using the 2D Smagorinsky option. Surface processes are calculating using the Noah land surface model (Barlage et al. 2010) with 24 land categories and 4 soil layers. Surface-layer exchange coefficients follow from Monin–Obukhov similarity as applied in the medium-range forecast (MRF) PBL scheme (Hong and Pan 1996).

### 4. Simulation results: Squall-line case

#### a. Baseline results with P3

Deep convection is initiated within the first 15 min of integration from the imposed low-level horizontal convergence. This leads to rapid development of heavy precipitation along the convergence line, with domain-maximum surface precipitation rates exceeding  $100 \text{ mm h}^{-1}$  within 30 min. Melting and evaporation of precipitation lead to the development of a cold pool at low levels. The interaction of the cold pool and low-level

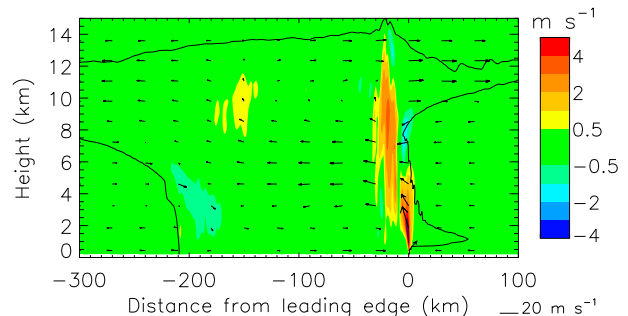


FIG. 3. Vertical cross sections of line-averaged vertical velocity (colored contours), 3D wind vectors, and region with condensate mass mixing ratio larger than  $0.01 \text{ g kg}^{-1}$  (black contour line) using the P3 scheme. Line averaging is performed relative to the location of the lowest-model-level gust front (defined by  $\theta' < -2 \text{ K}$ ). For plotting the wind vectors, vertical velocity is multiplied by a factor of 3 relative to horizontal velocity.

environmental shear leads to deep lifting of air along the cold pool edge. As the cold pool strengthens over time, the storm begins to propagate downshear, reaching grid-relative speeds of  $5\text{--}7 \text{ m s}^{-1}$  after 3 h.

After about 4 h, the simulated storm reaches a quasi-steady mature phase with dynamical characteristics typical of midlatitude squall lines with trailing stratiform precipitation (e.g., Biggerstaff and Houze 1993). Strong ascent associated with deep convective updrafts occurs near the surface gust front, with notable upshear tilting of convective drafts (Fig. 3). There are also regions of midlevel (4–12-km height) mesoscale ascent with vertical velocities of  $0.2\text{--}0.7 \text{ m s}^{-1}$  and low-level mesoscale descent of a similar magnitude in the trailing stratiform region. Ascending front-to-rear flow occurs throughout the storm at midlevels, with descending rear-to-front flow at lower levels behind the surface gust front. Divergence at upper levels in the convective region leads to substantial upper-level shear ahead of the storm and the formation of a forward anvil.

Cloud macrophysical and microphysical features are strongly influenced by these dynamical features and, in turn, influence them. Horizontal cross sections of the reflectivity at a height of about 1.1 km and 6 h, during the mature phase of the simulated storm, show a distinct region of high reflectivity ( $>45 \text{ dBZ}$ ) approximately 20–30 km wide associated with the leading edge of deep convection (Fig. 4a). This is followed (relative to the surface gust front) by an approximately 160-km-wide region of trailing stratiform precipitation with reflectivities mostly between 30 and 40 dBZ. These features are consistent with the observed reflectivity (cf. Figs. 4a and 1a), although the simulated low-level reflectivity in the trailing stratiform region is about 3–5 dBZ lower on average. The region of relatively weak

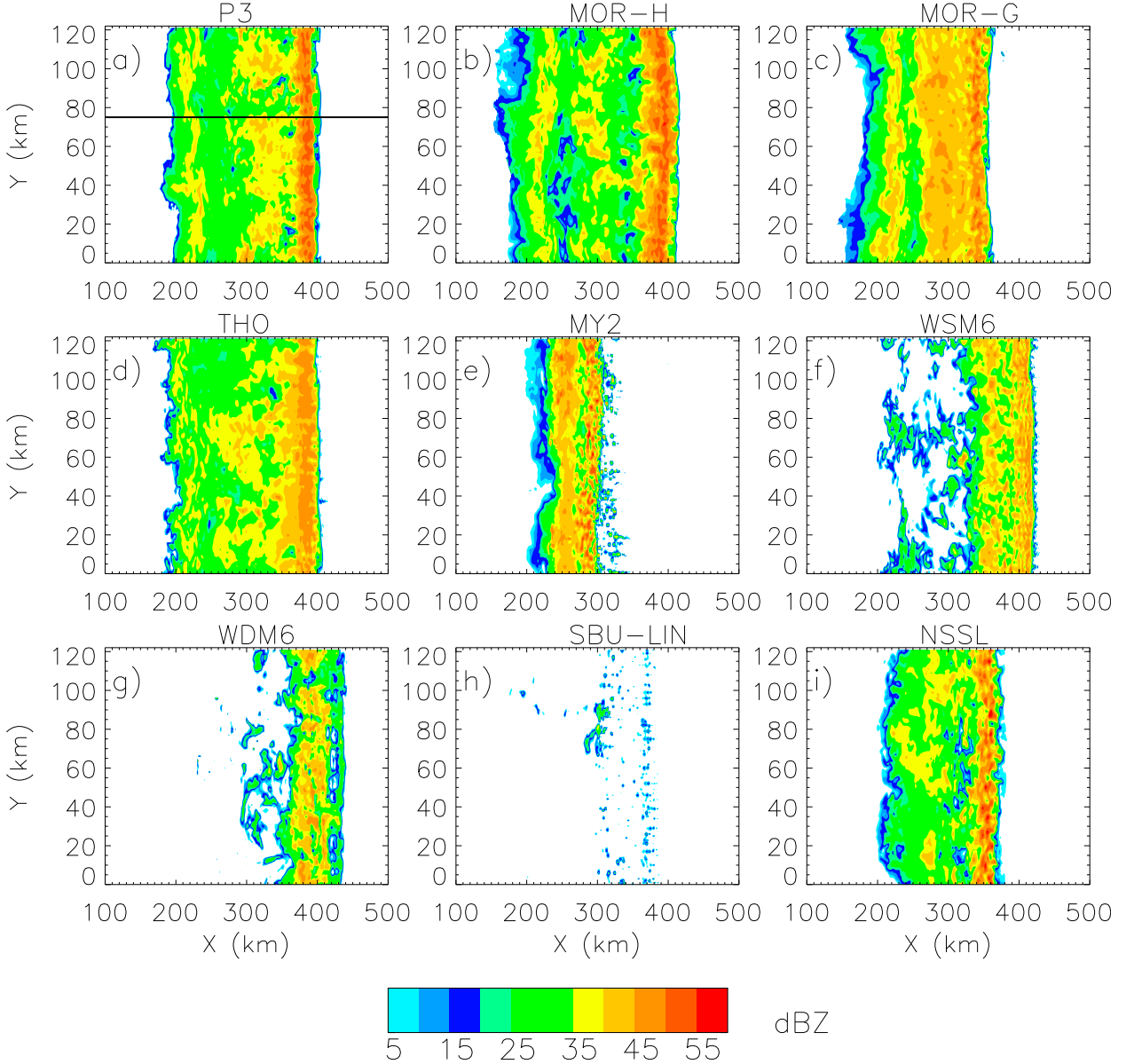


FIG. 4. Horizontal cross sections of radar reflectivity at 6 h and a height of  $\sim 1.1$  km from the WRF simulations using various microphysics schemes. (a) The horizontal line indicates the location of vertical cross sections shown in Fig. 6.

reflectivity in the transition region between the convective and trailing stratiform precipitation regions clearly seen in the observations is also less apparent in the simulation. A line-averaged vertical cross section of reflectivity reveals a low bias above 7 km in the convective region of 5–10 dBZ and a high bias just upshear of the convective region above 4 km of up to about 10 dBZ (cf. Figs. 5a and 1b), but most features are well simulated in both structure and magnitude. Note that the effects of wet ice on reflectivity are not included in the model, so it is not able to produce the distinct bright

band just below the freezing level ( $\sim 4$  km) seen in the observations.

Microphysical features simulated by P3 are illustrated by vertical cross-sectional plots of various quantities at 6 h (Fig. 6). A single transect perpendicular to the line (with location indicated in Fig. 4a) is used to illustrate detailed structure. Results are generally consistent with the idealized 2D squall-line simulations described in Part I. There is considerable cloud and rainwater in convective updrafts along the leading storm edge, with scattered cloud water at heights of 4–7 km in the trailing

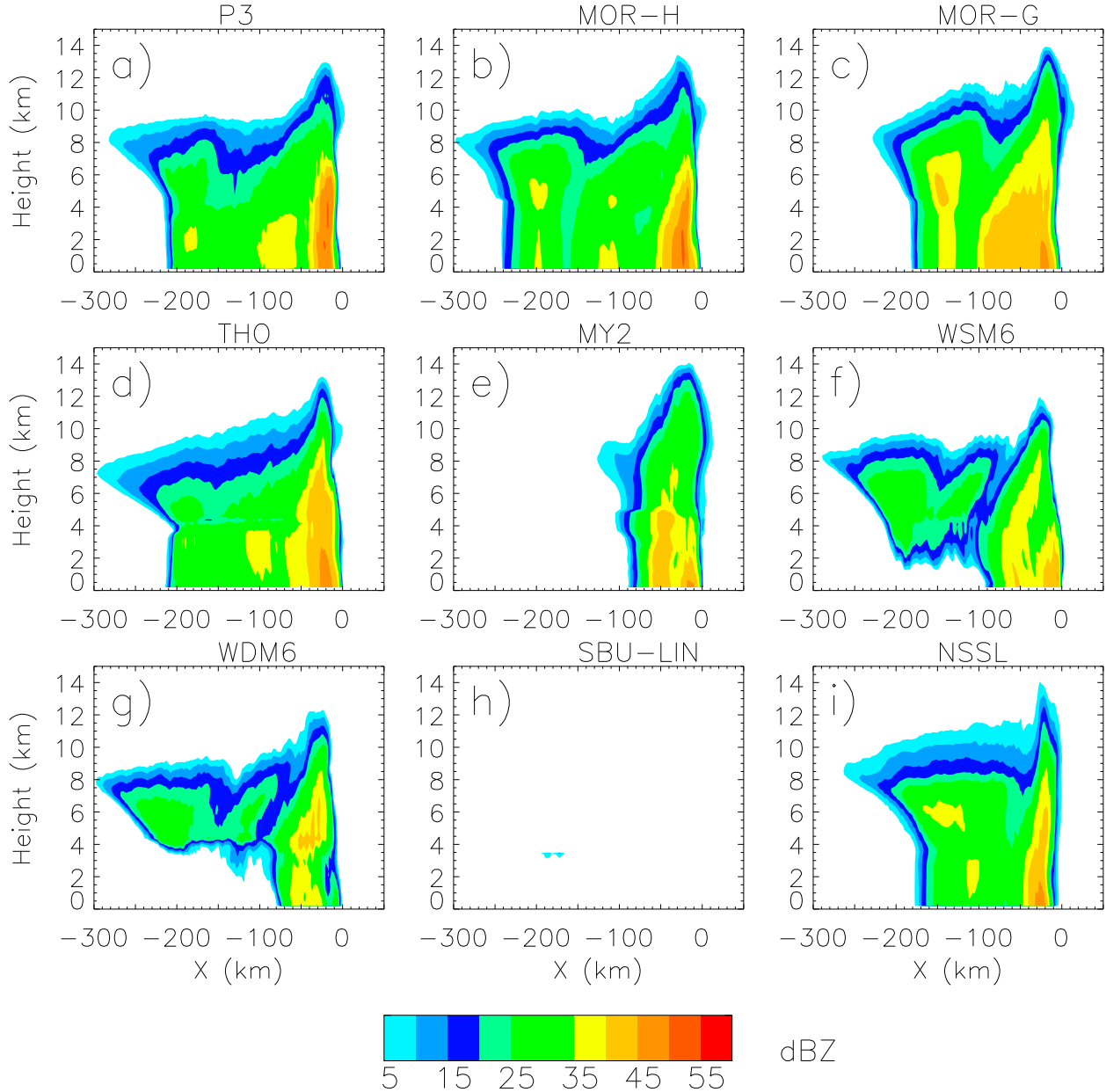


FIG. 5. Vertical cross sections of line-averaged reflectivity at 6 h from the WRF simulations using various microphysics schemes. Line averaging is performed relative to the location of the lowest model-level gust front (defined by  $\theta' < -2$  K).

stratiform region. There is also a region of low-level cloud water (1–2-km height) just ahead of the convective line associated with ascent along the gust front, analogous to a shelf cloud. In terms of ice particle properties, the rime mass fraction  $F_r$  is largest in and near convective updrafts, with large amounts of liquid water and, hence, riming. However, there are also regions with substantial rime mass at a considerable distance ( $>100$  km) from any liquid water. For example,  $F_r$  is generally between 0.1 and 0.3 near the anvil top

between  $X \sim 100$  and 300 km despite the lack of liquid water in this region. This occurs because of detrainment and horizontal transport of rimed ice from convective updrafts. The mass-weighted mean ice particle density  $\rho_p$  is largest in two regions: 1) near cloud top associated with mass-weighted mean ice particle size  $D_m < 100 \mu\text{m}$  (small particles are assumed to be ice spheres with  $\rho_p = 900 \text{ kg m}^{-3}$ ; see Part I) and 2) below 8 km in the convective region associated with large ( $D_m > 5 \text{ mm}$ ), high-density ( $\rho_p > 800 \text{ kg m}^{-3}$ ) rimed ice with mass-weighted

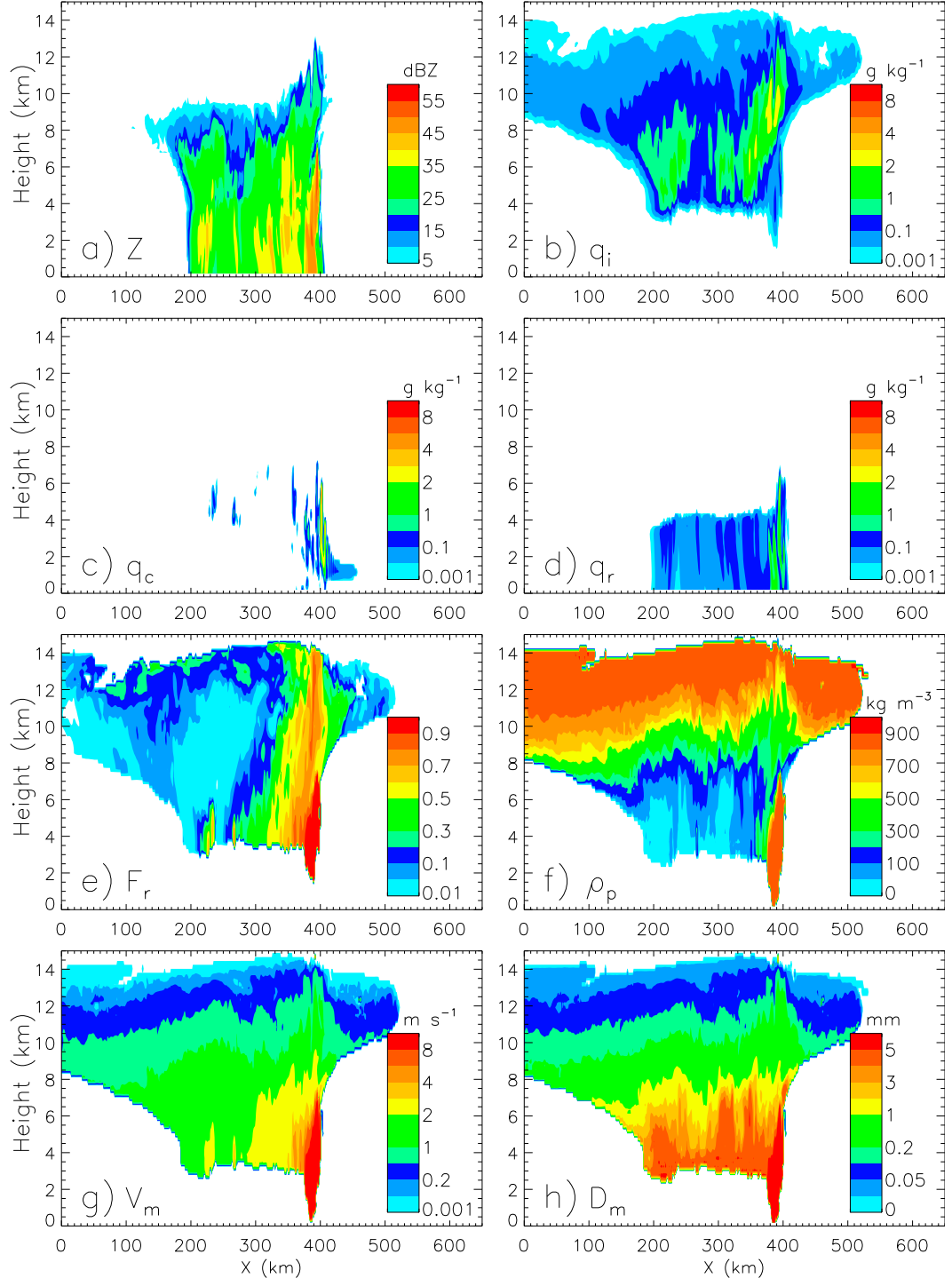


FIG. 6. Vertical cross sections of (a) radar reflectivity, (b) total ice mass mixing ratio, (c) cloud water mass mixing ratio, (d) rain mass mixing ratio, (e) rime mass fraction, (f) mass-weighted mean ice particle density, (g) mass-weighted mean ice particle fall speed, and (h) mass-weighted mean ice particle size at 6 h using the P3 scheme. The cross-section location is shown in Fig. 4a.

mean ice fall speed  $V_m$  generally larger than  $5 \text{ m s}^{-1}$ , resembling hail. The value of  $\rho_p$  is smallest below 6 km in the rearward part of the trailing stratiform region, associated with large ( $D_m > 3 \text{ mm}$ ), unrimed, or lightly rimed ice and  $V_m \sim 1\text{--}1.6 \text{ m s}^{-1}$ . Between the convective and trailing stratiform regions is a region with  $F_r$  between 0.4 and 0.8,  $\rho_p$  between 50 and  $250 \text{ kg m}^{-3}$ ,  $D_m > 1 \text{ mm}$ , and  $V_m$  between 2 and  $4 \text{ m s}^{-1}$ , resembling low- and medium-density graupel. This structure of ice particle properties is broadly consistent with ice particle types inferred from midlatitude squall-line radar observations and diagnostic studies (e.g., Rutledge and Houze 1987; Houze et al. 1989; Biggerstaff and Houze 1991, 1993; Braun and Houze 1994).

### b. Comparison of microphysics schemes

While eight of the nine microphysics schemes tested here produce a long-lived squall line, they produce a wide range of storm structure. This result is illustrated by comparing horizontal and line-averaged vertical cross-sectional plots of reflectivity for each simulation (Figs. 4 and 5). Results show a distinct grouping, with five of the nine schemes (P3, MOR-H, MOR-G, THO, and NSSL) producing a wide region (at least 150 km) of trailing stratiform precipitation and three of the nine (MY2, WSM6, and WDM6) producing little stratiform precipitation (particularly below the melting level). The squall line in SBU-LIN is not maintained and rapidly dissipates within the first 2 h. An explanation is the small  $V_m$  of precipitating ice particles; at 1 h values are generally less than  $3 \text{ m s}^{-1}$  above the freezing level (not shown), while in P3 at 1 h the  $V_m$  are 2–3 times larger in many locations. As a result, there is limited precipitation falling into the melting layer in the SBU-LIN simulation, leading to a very weak cold pool that is not able to initiate secondary convection and maintain the storm (these results are discussed further below). We note that SBU-LIN was initially developed in the context of wintertime orographic precipitation (Lin and Colle 2011), and it produces results that are much closer to observations for the IMPROVE-2 orographic precipitation case discussed later.

There are large differences in the reflectivity structure even among schemes that produce substantial trailing stratiform precipitation. For example, MOR-G, which assumes graupel for the rimed-ice species, produces a high-reflectivity convective region that is 70–90 km wide, or 3 times as wide as simulated by P3 and NSSL, or observed. WSM6 and WDM6, which also assume graupel for the rimed-ice category, and MY2, which includes separate categories for graupel and hail but for which graupel dominates in terms of overall mass (Fig. 7), also produce wide, relatively indistinct high-reflectivity

regions associated with the leading-edge convection. On the other hand, MOR-H, which assumes hail for the rimed-ice species, and NSSL, which includes separate categories for graupel and hail and produces substantial amounts of hail (Fig. 7), simulate a much narrower (25–50 km) and more distinct convective region with a reflectivity structure that is closer to observations. P3 simulates a reflectivity structure in the convective region broadly similar to MOR-H and NSSL because of its prediction of ice with hail-like characteristics—in particular,  $V_m > 5 \text{ m s}^{-1}$  (see Fig. 6g). Despite overall similarity with MOR-H and NSSL, P3 has some notable improvements including reflectivities above the freezing level in the trailing stratiform region that are up to 10 dBZ lower. This is partly attributed to the assumption of spherical snow with a fixed bulk density of  $100 \text{ kg m}^{-3}$  in MOR-H and NSSL, compared to the variable bulk density in P3 (see Fig. 6f). Relative to MOR-H, P3 produces a 10–15-km narrower high-reflectivity convective region and a more continuous region of high reflectivity along the leading edge of convection compared to NSSL. However, MOR-H and NSSL produce a more realistic area of low reflectivity in the transition between the stratiform and convective regions.

THO, which employs a hybrid approach to treat graupel and hail, gives a reflectivity structure between the graupel- and hail-dominant schemes. It produces a narrower convective region than MOR-G, MY2, WDM6, and WSM6 but still wider and with lower reflectivities than in MOR-H, P3, NSSL, and the observations. It also produces a less distinct transition between the convective and trailing stratiform regions, with a wide area of reflectivities between 35 and 45 dBZ. However, it produces reflectivities in the convective region above 7 km up to 10 dBZ larger than MOR-H or P3 that better match with observations and a somewhat more realistic reflectivity structure in the trailing stratiform region.

Sensitivity to the treatment of rimed ice appears to be primarily driven by differences in fall speed. For example, a simulation with MOR-H but using the fall speed-size relationship for graupel instead of hail (MOR-H-F) is similar to MOR-G. This result is consistent with Bryan and Morrison (2012) and Morrison and Milbrandt (2011), who examined specification of hail versus graupel for squall-line and supercell simulations, respectively. This point is further demonstrated by a sensitivity test with P3 but with an ice fall speed that is not allowed to be greater than the fall speed-size relationship for graupel used in MOR-G and MY2 (P3-F). This test produces a wide and relatively indistinct region of high reflectivity along the leading storm edge more similar to the graupel-dominant schemes (not shown).

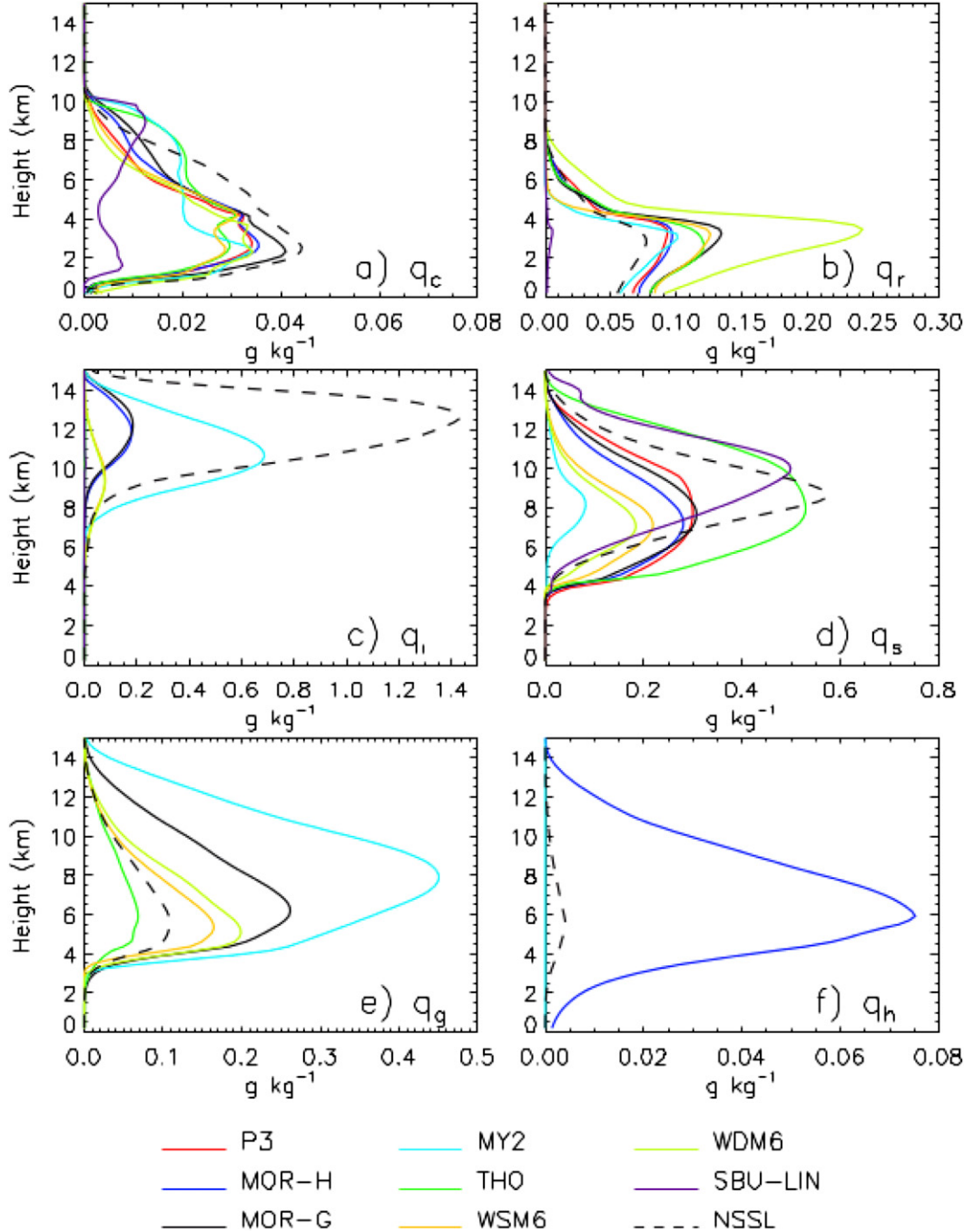


FIG. 7. Horizontally and temporally averaged (from 6 to 7 h) profiles of (a) cloud water mass mixing ratio, (b) rain mass mixing ratio, (c) cloud ice mass mixing ratio, (d) snow mass mixing ratio, (e) graupel mass mixing ratio, and (f) hail mass mixing ratio. The P3 ice mass mixing ratio is shown in (c). Note that the *x* axis scales are different among the plots.

For the group of schemes that produces a weak or nonexistent trailing stratiform region, WSM6 and WDM6 produce significant stratiform precipitation aloft, but it is rapidly evaporated below the melting level. This is explained by the small mean raindrop size produced by

these schemes as discussed below. On the other hand, MY2 produces little trailing stratiform precipitation either above or below the freezing level. This is consistent with snow mass mixing ratios aloft that are about 2–6 times smaller compared with the other simulations

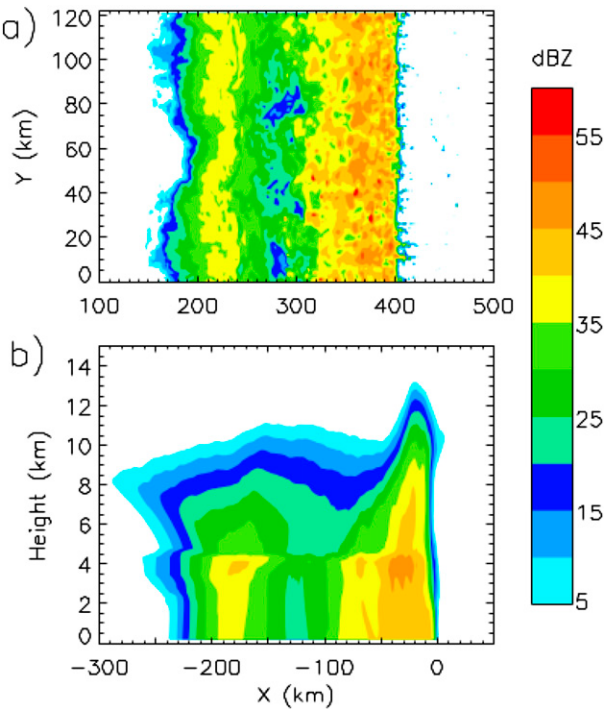


FIG. 8. As in Figs. 5 and 6, but for (a) horizontal and (b) line-averaged vertical cross sections of radar reflectivity at 6 h for the modified MY2 scheme.

(Fig. 7d), which is due to a known bias in the MY2 scheme that produces too much cloud ice and excessively broad and thick anvils (Cintineo et al. 2014). There is also very little hail compared with graupel (Figs. 7e,f), which results in a relatively weak convective region indicated by the low-reflectivity values (Figs. 4e and 5e). These biases have been largely corrected in a recent version<sup>1</sup> of MY2 (available in WRF, version 3.6), which now produces much less cloud ice, more snow, and more hail. Simulations of this case using the modified MY2 produce results that are qualitatively similar to the first group of schemes, with a distinct trailing stratiform region, high-reflectivity convective core, and a faster propagation speed (Fig. 8).

NSSL gives the largest cloud ice mass mixing ratios among all schemes and large average snow mixing ratios aloft that exceed  $0.55 \text{ g kg}^{-1}$  (Figs. 7c,d). Since snow and cloud ice have low mean fall speeds compared with graupel or hail, this limits the flux of ice into the melting layer and production of rain in NSSL, and it has the smallest rain mass mixing ratios except for SBU-LIN

(Fig. 7b). Overall, large differences in the mass mixing ratio profiles for the ice-phase categories (cloud ice, snow, graupel, and hail) seen in Fig. 7, often exceeding several orders of magnitude, highlight the inherent uncertainty in conversion rates between predefined ice-phase categories that motivated the development of P3.

A comparison of time-averaged (6–7 h) and line-averaged precipitation rate at a height of 1.1 km from the simulations and radar retrieval is shown in Fig. 9 (note the modeled surface precipitation rate is similar to that at 1.1 km). These results are generally consistent with the reflectivity structure described above. The graupel-dominant schemes (MOR-G, MY2, WSM6, and WDM6) produce a wide, broad region of high precipitation with a maximum precipitation rate about one-half of that retrieved. Three of these schemes (MOR-G, MY2, and WSM6) produce a distinct secondary peak in the precipitation rate well behind (50–60 km) the surface gust front, while in WDM6 the maximum rate is located 60 km behind the surface gust front. P3, MOR-H, and NSSL simulate peak precipitation rates about 1.5–3 times larger compared to the other schemes, with magnitudes and locations (relative to the leading edge of precipitation) similar to the retrieval. This results primarily from the specification of rimed ice as hail in MOR-H, inclusion of a separate hail category and substantial production of hail in NSSL, and the prediction of ice with hail-like characteristics in the convective region in P3, leading to fast-falling ice near the leading edge of the storm compared to slower-falling ice in the other schemes. This is shown by the two sensitivity tests described above with reduced fall speed (MOR-H-F and P3-F), which both produce results that are similar to MOR-G with a relatively small peak convective precipitation rate, especially for MOR-H-F (Fig. 10). THO, with its hybrid representation of hail and graupel, produces a somewhat higher peak precipitation rate than MOR-G, WSM6, WDM6, or MY2 but substantially less than P3, MOR-H, or NSSL (Fig. 9). There are also notable differences in the transition between heavy convective precipitation and much lighter trailing stratiform precipitation between P3, THO, NSSL, and MOR-H. P3, NSSL, and MOR-H simulate a sharp reduction of precipitation rate behind the leading edge of convection, with P3 producing a local minimum between the convective and stratiform regions that is similar in magnitude and location to the retrieval. In contrast, THO produces a wider transition in precipitation rates between the convective and stratiform regions consistent with the reflectivity structure described above. All schemes underpredict the precipitation rate in the trailing stratiform region, especially for locations 100–170 km behind the surface gust front. This could be due

<sup>1</sup>The modified MY2 scheme was not available in the official WRF, version 3.4.1, library, from which all the schemes tested in this study (except P3) were taken. The changes to MY2 are summarized in section a of the appendix.

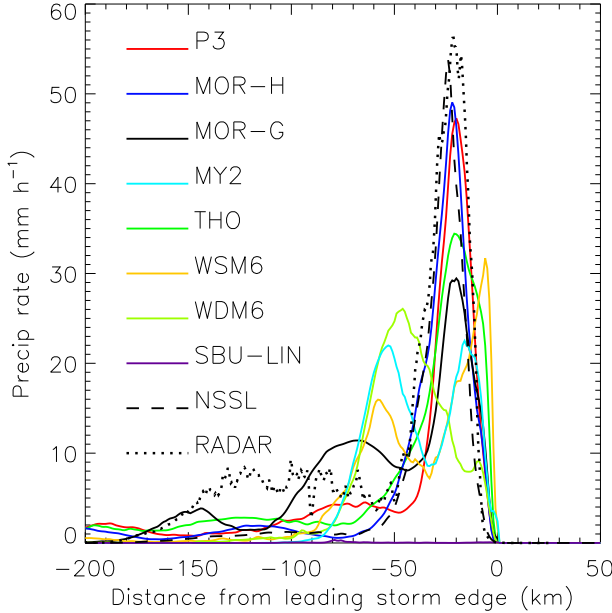


FIG. 9. Line-averaged cross sections of precipitation rate at a height of  $\sim 1.1$  km from the simulations and radar retrieval. Simulated values are time averaged from 6 to 7 h. Line averaging is performed relative to the location of the lowest-model-level gust front (defined by  $\theta' < -2$  K).

to several factors in addition to microphysics, such as uncertainty in the environmental conditions (e.g., vertical wind shear), relatively coarse grid resolution, or neglect of radiation.

Raindrop size is important because it strongly affects sedimentation and evaporation and, hence, cold pool evolution and surface precipitation. Figure 11 shows line-averaged vertical cross sections of the modeled (at 6 h) and retrieved drop median volume diameter  $D_0$ . Figure 12 shows a comparison of the line-averaged modeled and retrieved  $D_0$  with point measurements from the surface disdrometer (note the retrieved values in Fig. 12 are at a height of about 0.6 km). For the two-moment schemes,  $D_0$  is derived from the predicted rain number and mass mixing ratios and size distribution shape parameters. For the one-moment WSM6 scheme,  $D_0$  is derived from the predicted rain mass mixing ratio and specified  $N_0$ . ( $D_0$  is not analyzed for the one-moment SBU-LIN scheme since it does not produce a long-lived squall line.) While the overall trend of  $D_0$  as a function of distance from the leading edge of the storm is similar between the retrievals and disdrometer, the magnitudes differ substantially. This is potentially due to several factors, including different heights, retrieval and disdrometer measurement uncertainty, and 3D variability within the storm that is averaged out for the line-averaged radar-retrieved  $D_0$ . To varying degrees

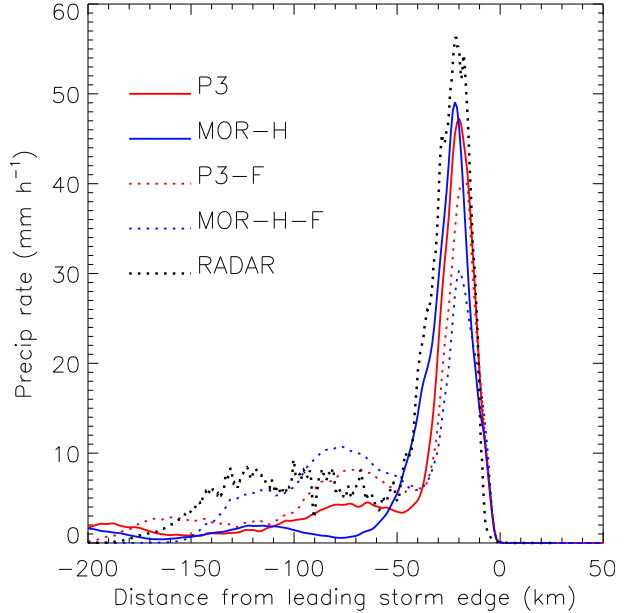


FIG. 10. As in Fig. 9, but for a comparison of retrieved and modeled precipitation rates for MOR-H, P3, and the sensitivity tests using these schemes with modified fall speed, MOR-H-F and P3-F, respectively.

P3, MOR-H, MOR-G, MY2, THO, and NSSL all overpredict  $D_0$ , except in the convective region near the leading storm edge, compared to the disdrometer. This is likely due to excessive size sorting, which is partly mitigated in some schemes using various methods as explained below. In contrast, WSM6 and WDM6 generally underpredict  $D_0$ , especially in the trailing stratiform region. The small  $D_0$  in these schemes is consistent with rapid evaporation and the decrease of reflectivity with height in the trailing stratiform region seen in Figs. 5f and 5g, since rain evaporation increases with decreasing  $D_0$  (all else being equal). The small  $D_0$  in WSM6 is explained by the large  $N_0$  specified in the scheme compared to that predicted by the two-moment schemes except WDM6. This is consistent with previous studies showing large evaporation rates and limited stratiform precipitation at the surface using one-moment schemes with a similar specification of  $N_0$  (Morrison et al. 2009; Luo et al. 2010; Bryan and Morrison 2012). Explanations for the small  $D_0$  in WDM6 are less clear but may be related to coupling of the liquid and ice microphysics.

Another notable bias is that MOR-H, MOR-G, and MY2 produce a substantial decrease of  $D_0$  with height in the trailing stratiform region, from greater than 2 to about 1 mm, while the radar retrievals show nearly constant  $D_0$ . This is likely explained by the fixed exponential size distributions assumed by these schemes,

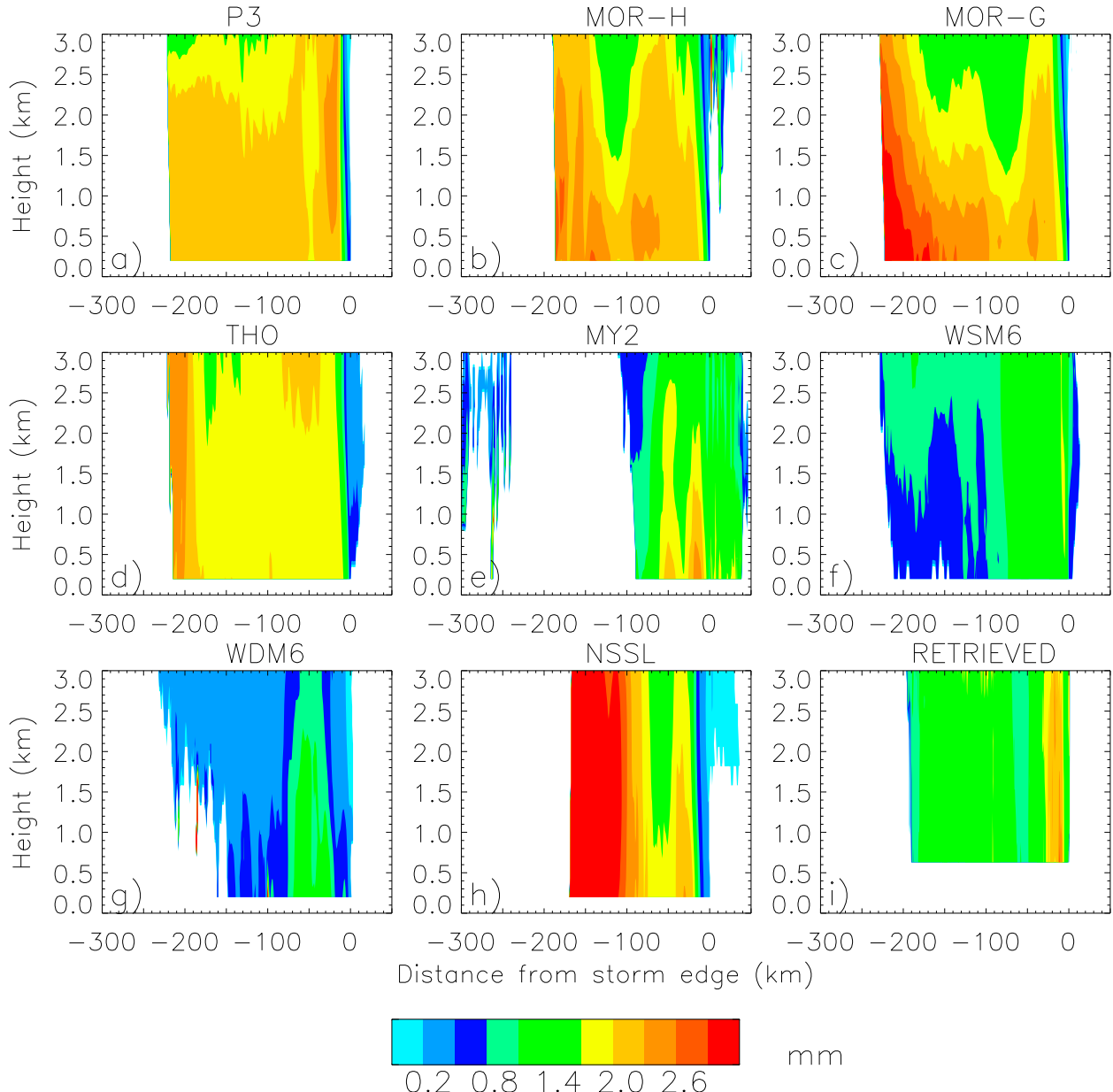


FIG. 11. Line-averaged vertical cross sections of  $D_0$  for the different simulations at 6 h and the radar retrieval. Line averaging is performed relative to the location of the lowest-model-level gust front (defined by  $\theta' < -2\text{ K}$ ). Locations with rain mass mixing ratio  $\geq 0.01\text{ g kg}^{-1}$  are conditionally sampled for the modeled line-averaged  $D_0$ .

which are known to result in excessive size sorting (Wacker and Seifert 2001; Milbrandt and Yau 2005a; Milbrandt and McTaggart-Cowan 2010). This is partly mitigated in P3 and WDM6 by the use of a rain DSD with a nonzero shape parameter as well as in P3 by a fairly stringent range of the rain slope parameter  $\lambda$  through the parameterization of drop breakup (see appendix C, section g in Part I). On the other hand, size sorting is limited in THO by an ad hoc reduction of differences in the number- and mass-weighted mean fall

speeds compared to the analytic calculations. Excessive size sorting is limited in NSSL by a correction scheme that adjusts number concentration to prevent spurious reflectivity growth (Mansell 2010), although it produces very large  $D_0$  in the trailing stratiform region. P3, MY2, and WSM6 are able to simulate the narrow peak in  $D_0$  in the convective region seen in the radar and disdrometer observations, while the other schemes produce their largest  $D_0$  more than 30–40 km behind the surface gust front.

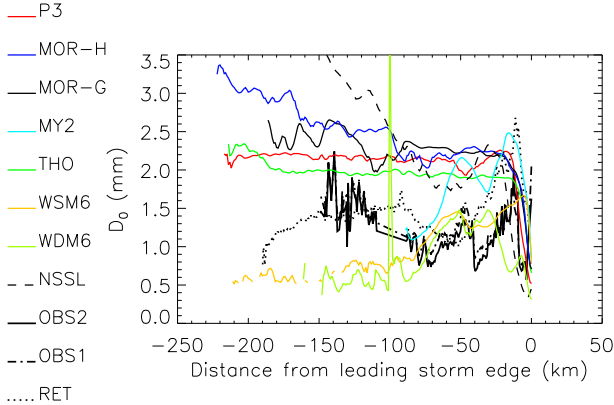


FIG. 12. As in Fig. 11, but for comparison of lowest-model-level  $D_0$  with disdrometer observations (OBS1 and OBS2) and the radar retrieval at a height of  $\sim 0.6$  km (RET). OB1 and OBS2 indicate  $D_0$  from disdrometer assuming exponential and gamma drop size distributions, respectively.

Differences in microphysics lead to a fairly large spread in the storm thermodynamic and dynamical characteristics, which is illustrated by time series of various quantities shown in Fig. 13. Overall, differences are much less after 5–6 h than before. P3 gives results that tend to lie in the middle range of simulations. Large rain evaporation rates in WSM6 and WDM6 are consistent with the small rain  $D_0$  discussed above (Fig. 13b).

As expected, there is a relationship between rain evaporation rates and cold pool strength. The latter is quantified by the cold pool intensity (Rotunno et al. 1988; Bryan et al. 2006), given by

$$C^2 = -2 \int_0^H B dz, \quad (3)$$

where  $z$  is height above the surface;  $B$  is the buoyancy that here includes contributions from temperature, vapor, and condensate; and  $H$  is the height of the cold pool defined as the level below which  $B < 0$ . Here  $C$  is taken as an average 0–30 km behind the surface gust front. There is also a close correspondence between larger  $C$  (Fig. 13c) and faster storm propagation (Fig. 13d), which is expected from density current theory (e.g., Rotunno et al. 1988). With the small mean fall speed of precipitating ice in SBU-LIN there is limited production of rainwater from melting, leading to limited rain evaporation (Fig. 13b) and hence a very weak cold pool and small  $C$  (Fig. 13c). As a result, there is little initiation of secondary convection and the squall line rapidly dissipates in this simulation.

Figure 13 also suggests a relationship between the cold pool and convective dynamical characteristics. In general, simulations with smaller  $C$  have a smaller

fraction of the domain with convective updrafts  $F_c$  and larger mass flux conditionally averaged within convective updrafts  $M_c$  at low and midlevels (illustrated in Figs. 13e and 13f at a height of 5 km). Here convective updrafts are defined using a threshold vertical velocity of  $2 \text{ m s}^{-1}$ . However, there is not a clear one-to-one relationship; THO is a notable exception in that it produces a relatively small  $C$  but has the largest  $F_c$  and smallest  $M_c$  after 3 h. Nonetheless, overall correspondence between  $C$ ,  $F_c$ , and  $M_c$  is consistent with the results of Morrison et al. (2012). They tested sensitivity for the same case (but with somewhat different environmental conditions) by systematically varying the raindrop breakup parameterization and also found that larger  $C$  was associated with larger  $F_c$  and smaller  $M_c$  in the lower and midtroposphere. These results are consistent with convective updrafts that are more tilted and weaker in simulations with larger  $C$ , in agreement with “RKW theory” (e.g., Rotunno et al. 1988; Weisman and Rotunno 2004; Bryan et al. 2006). A likely explanation for more scatter in the relationship between  $C$ ,  $F_c$ , and  $M_c$  here compared to Morrison et al. (2012) is that they only varied a single parameter that primarily affected cold pool evolution, whereas the schemes tested here have different representations of numerous processes and parameters that affect convective characteristics through several mechanisms.

Finally, we note that the squall line tends to develop more slowly with MOR-G and MY2. For example, these schemes do not develop  $C > 20 \text{ m s}^{-1}$  until 1.75 h, whereas all other schemes reach this threshold at 1 h (Fig. 13c). Propagation speed remains slower than all other schemes for the first 4 h with MOR-G and for the entire simulation with MY2. These differences are likely attributable to the small rain evaporation rates within the first 1.75 h compared to the other schemes (except SBU-LIN); for MOR-G this results from relatively slow-falling graupel, which remains above the melting layer longer and thus does not melt, and subsequently evaporate, until a later time.

## 5. Simulation results: Orographic precipitation case

### a. Baseline results with P3

WRF is able to capture reasonably the synoptic-scale evolution of the storm, which is strongly constrained by the initial conditions and lateral boundary forcing. It also reasonably predicts the horizontal wind field, temperature, and humidity structure in the IMPROVE-2 study area as indicated by the University of Washington soundings launched near Creswell, Oregon [see Figs. 7 and 8 in Garvert et al. (2005a) and Fig. 6 in Milbrandt

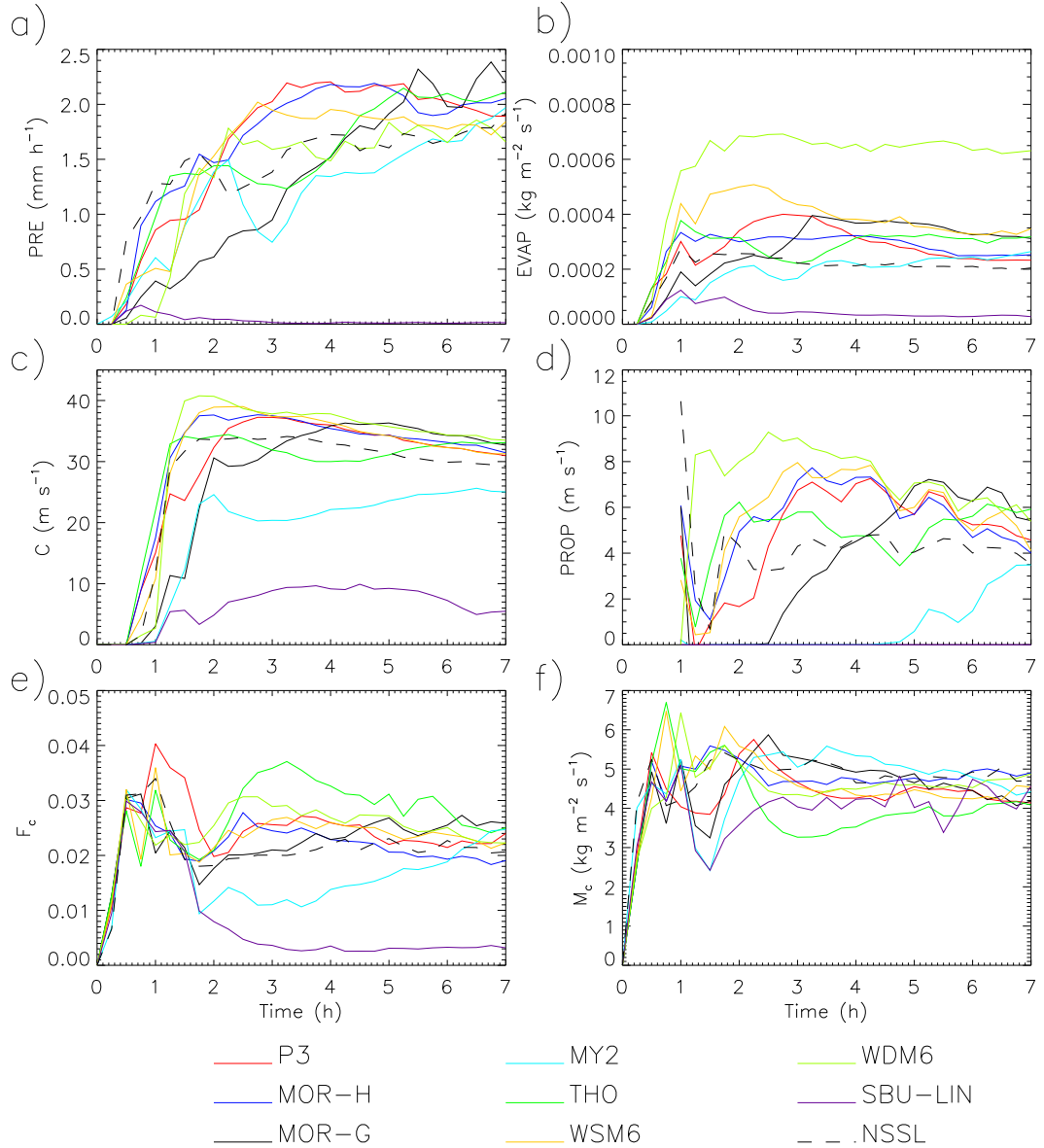


FIG. 13. Time series of (a) domain-averaged surface precipitation rate, (b) domain-averaged vertically integrated rain evaporation rate, (c) cold pool intensity averaged from 0 to 30 km behind the surface gust front, (d) gust front propagation speed, (e) fraction of the domain with convective updrafts, and (f) updraft mass flux conditionally sampled in convective updrafts. The terms in (e),(f) are at a height of  $\sim 5$  km.

et al. (2008)]. We note that biases are similar to Milbrandt et al. (2008), who simulated this case with the limited-area model configuration of the Global Environmental Multiscale (GEM) model but with the same initial conditions and lateral forcing. For example, the horizontal wind speed tends to be somewhat underpredicted between 700 and 800 hPa (e.g., 25–30 versus 35–40 m s<sup>-1</sup>). While these biases are noted, they are similar among all of the simulations; thus, the microphysics schemes are forced by similar dynamical fields.

Lowest-model-level reflectivity for the P3 simulation at 0000 UTC 14 December is shown in Fig. 14 along with observations from the KRTX radar at Portland, Oregon. P3 produces a reasonable reflectivity structure for the broader system (Fig. 14a). It also captures overall features seen in the observations over the IMPROVE-2 domain (Figs. 14b,c), including a large stratiform precipitation region associated with the main frontal system to the south and east of Portland, Oregon, and showery, postfrontal precipitation to the north and west. However, the modeled reflectivity tends to be higher

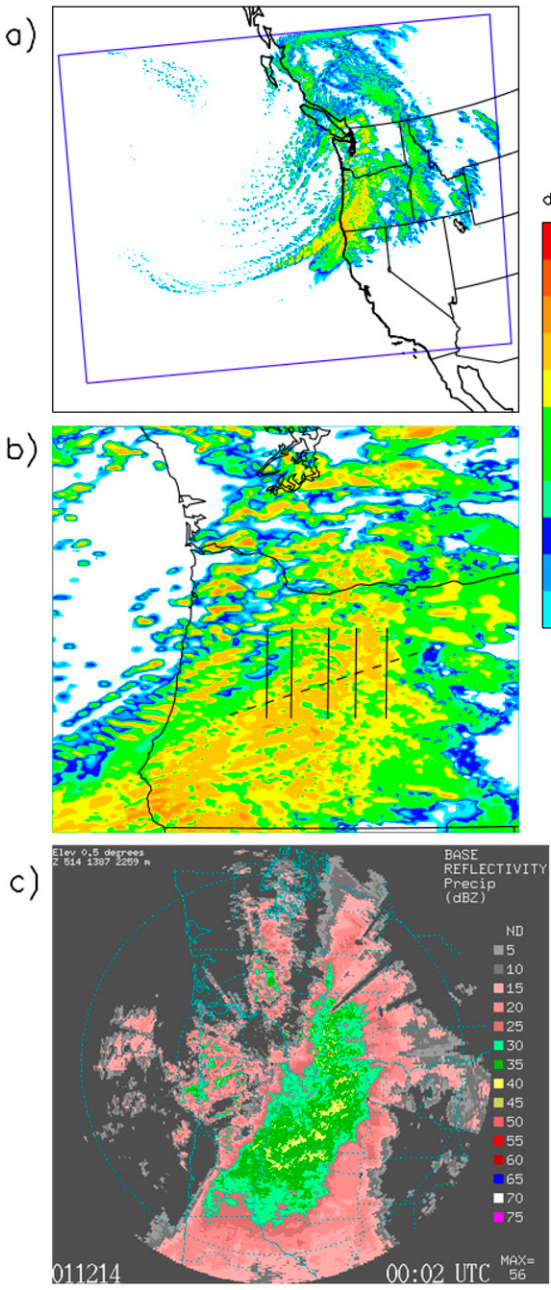


FIG. 14. Radar reflectivity at  $\sim 0000$  UTC 14 Dec for (a) lowest model level across the full model domain shown by the blue lines, (b) lowest-model-level reflectivity for the IMPROVE-2 region, and (c) WSR-88D ( $0.5^\circ$  PPI) at Portland, Oregon. The approximate north-south P-3 flight tracks (solid lines) and southwest-northeast Convair transect (dashed line) are shown in (b).

than observed, especially for the postfrontal showers where the model produces instances of reflectivity exceeding  $45\text{ dBZ}$  while the Portland radar shows few values greater than  $40\text{ dBZ}$ . Simulations using the other schemes (not shown) exhibit similar reflectivity

structures, although WSM6 and especially WDM6 produce much lower reflectivity values. However, quantitative comparison is challenging because of issues such as terrain blocking and bright-band enhancement associated with melting ice hydrometeors (which is neglected in the model).

Microphysical structure simulated by the P3 scheme is illustrated by vertical cross sections of various quantities along the southwest–northeast Convair transect at 0000 UTC 14 December (Fig. 15). Orographic ascent driven by the strong cross-barrier flow in the lower troposphere results in the production of large amounts of condensate between the Willamette Valley and Cascade ridgeline. The peak ice mass mixing ratio  $q_i$  occurs approximately  $30\text{ km}$  upwind of the ridgeline, with a rapid decrease of  $q_i$  in the descending motion downwind (east) of the ridgeline. There is extensive cloud liquid water with mass mixing ratios up to about  $0.5\text{ g kg}^{-1}$  on the windward side of the Cascades below about  $450\text{ hPa}$ , mainly in areas of ascent. This leads to considerable riming of ice at lower levels, with  $F_r$  locally exceeding 0.4 between  $750$  and  $850\text{ hPa}$ . The presence of rimed ice and graupel on the windward slope of the Cascades below about  $600\text{ hPa}$  is consistent with aircraft observations (Garvert et al. 2005a) and polarimetric radar observations (Houze and Medina 2005). However,  $\rho_p$  is fairly low because there is little wet growth or rain above the freezing level (which is assumed to yield high-density ice upon heterogeneous freezing or riming in P3; see Part I). Thus, while there is an increase in  $\rho_p$  in regions with rimed compared to unrimed ice at a given vertical level, peak values are generally less than  $100\text{ kg m}^{-3}$ . Nonetheless, there is a notable increase in  $V_m$  in regions with significant rimed ice and hence large  $F_r$  compared to elsewhere ( $V_m \sim 1.6\text{--}2.3\text{ m s}^{-1}$  versus less than  $1.6\text{ m s}^{-1}$ ). This has important implications for the distribution of surface precipitation as described in the next subsection.

#### b. Comparison of microphysics schemes

With all of the schemes, the simulations have a similar overall storm evolution and dynamical forcing for the microphysics in the IMPROVE-2 domain. The latter is evident by similar wind fields and thermodynamic soundings. For example, differences in temperature and  $u$  and  $v$  winds among simulations at all levels between the surface and  $300\text{ hPa}$ , averaged from 2300 UTC 13 December to 0100 UTC 14 December along the Convair flight track (i.e., the dashed line shown in Fig. 14b), are less than  $1.3\text{ K}$  and  $3.3\text{ m s}^{-1}$ , respectively. However, there are notable differences in microphysical quantities and distributions of surface precipitation (herein all surface precipitation amounts presented are liquid equivalent). The latter is demonstrated by

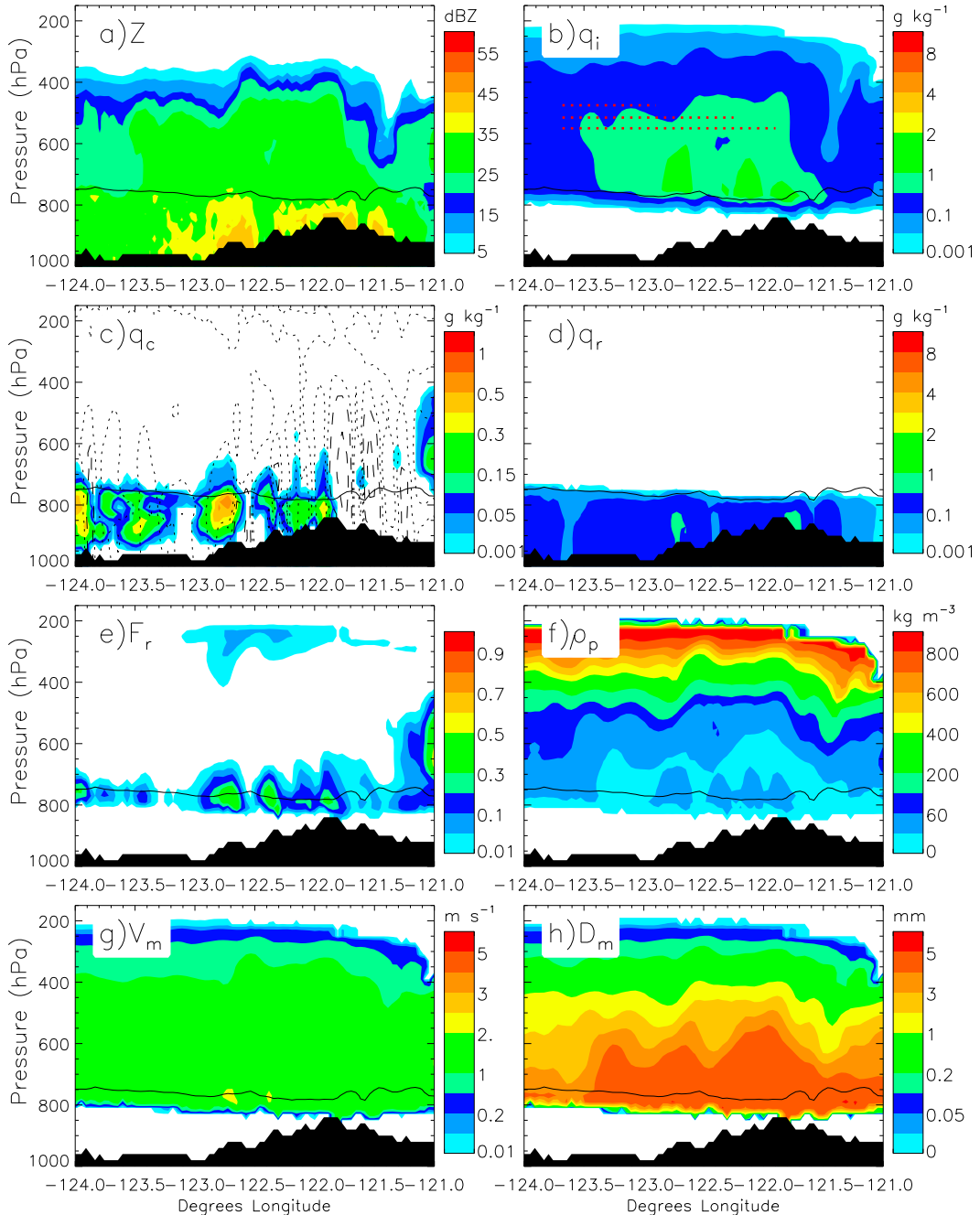


FIG. 15. Vertical cross section of (a) radar reflectivity, (b) total ice mass mixing ratio, (c) cloud water mass mixing ratio (color contour), and vertical velocity (contour lines plotted for  $-2.5, -1.5, -0.5, 0, 0.5, 1.5, 2.5 \text{ m s}^{-1}$ ;  $w < 0 \text{ m s}^{-1}$  dashed line,  $w \geq 0 \text{ m s}^{-1}$  dotted line), (d) rain mass mixing ratio, (e) rime mass fraction, (f) mass-weighted mean ice particle density, (g) mass-weighted mean ice particle fall speed, and (h) mass-weighted mean ice particle size at 0000 UTC 14 Dec using the P3 scheme. The cross-sectional location along the southwest–northeast Convair flight track is shown in Fig. 14b. Locations of the three Convair flight legs in Table 3 are shown by red dashed lines in (b). The freezing-level isotherm is shown in all panels by the solid line.

comparing the 1400 UTC 13 December with 0800 UTC 14 December accumulated precipitation among schemes. We also compare simulated precipitation with observations at the station locations shown in Fig. 16. A map of

accumulated precipitation simulated by P3 with the station observations is presented in Fig. 17. The model is able to simulate overall features of the precipitation distribution, with the highest values in the central Oregon

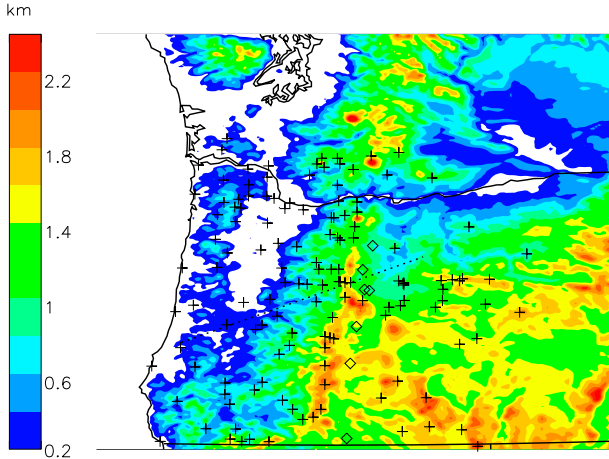


FIG. 16. Surface elevation (color contours) and location of the surface precipitation station observations (plus signs); stations in the immediate lee of the Cascades (station subset “LEE” in Table 1) are shown by diamonds.

Cascades and significantly less in the lee of the Coast Range and especially east of the Cascades, where accumulated precipitation is generally less than 10 mm. The most apparent biases are along the central and southern Oregon Cascades crest. However, some station measurements at higher altitudes likely underestimated precipitation amounts owing to various known issues during snowfall including undercatchment from wind over the gauge and riming on the rim, depending upon the particular instrument and setup (Rasmussen et al. 2012). For example, some of the University of Washington tipping-bucket gauges appear to have suffered from undercatchment; little accumulation was measured at the Santiam Junction and Corbett SnoPark sites after the transition from rain to snow, despite significant continued accumulation at nearby sites where the precipitation remained as rain. The SNOTEL sites with all-weather weighing gauges may be less prone to undercatchment, but all gauges may be problematic to varying degrees under strong wind conditions (Rasmussen et al. 2012).

Mean and root-mean-square error (RMSE) accumulated precipitation relative to all of the station observations is shown in Table 1. Simulated precipitation is linearly interpolated from the model grid to the station locations. Because of issues with undercatchment of snowfall, we also show a comparison in Table 1 that excludes stations that likely experienced significant snow accumulation (i.e., the subset of only “warm” stations). These stations were identified by locations colder than 0°C at 0800 UTC 14 December in the P3 simulation, which is reasonable given the accurate prediction of temperature soundings by the model. Mean

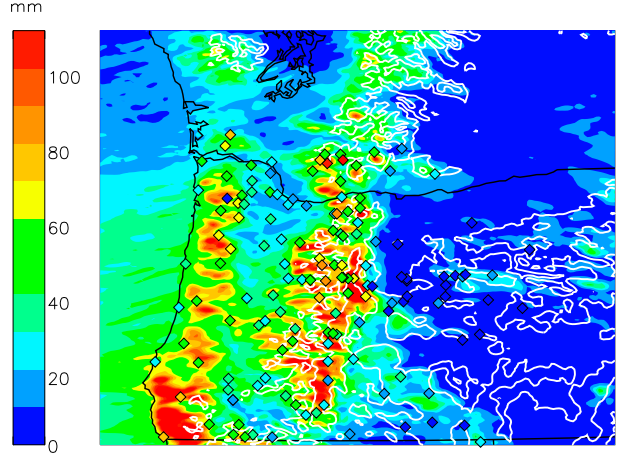


FIG. 17. Accumulated surface precipitation from the P3 simulation overlaid with station surface observations (diamonds) from 1400 UTC 13 Dec to 0800 UTC 14 Dec. White contour lines show surface elevation at heights of 1 and 1.5 km.

and RMSE accumulated precipitation are shown in the rightmost columns in Table 1 for the seven stations in the immediate lee of the Cascades (locations for these stations are shown by diamonds in Fig. 16). All simulations tend to overpredict precipitation for stations with less than 10 mm, including in the lee of the Cascades, and underpredict for stations with greater than 60 mm. SBU-LIN gives the lowest RMSE for all stations, which is consistent with a lower mean precipitation rate.

Figure 18 shows maps of the precipitation differences for each scheme relative to P3. Accumulated surface precipitation is also shown along the Convair cross section from the Willamette Valley across the Cascade Range for each scheme in Fig. 19. A few broad trends

TABLE 1. Comparison of statistics of accumulated surface precipitation (mm) from 1400 UTC 13 Dec to 0800 UTC 14 Dec for the simulations and station observations. “ALL” includes all stations, “WARM” excludes stations with likely snow accumulation, and “LEE” includes the seven stations shown in Fig. 16 in the immediate lee of the Cascades.

	ALL		WARM		LEE	
	Mean	RMSE	Mean	RMSE	Mean	RMSE
Obs	35.7	—	34.7	—	17.7	—
P3	45.1	16.3	40.1	11.9	35.1	17.9
MY2	46.9	17.6	41.5	12.7	50.0	32.3
MOR-G	47.3	18.6	42.9	13.2	58.5	40.9
MOR-H	47.2	19.3	43.2	15.1	58.8	41.1
NSSL	43.3	16.5	40.6	14.9	41.7	24.0
SBU-LIN	41.0	14.7	35.7	11.0	37.5	19.8
THO	44.6	17.0	39.9	13.2	35.4	18.0
WSM6	45.9	16.6	38.8	11.0	39.1	21.4
WDM6	45.2	17.0	37.2	11.1	21.3	5.5
P3-MOD	47.1	18.5	41.3	13.7	45.3	27.7

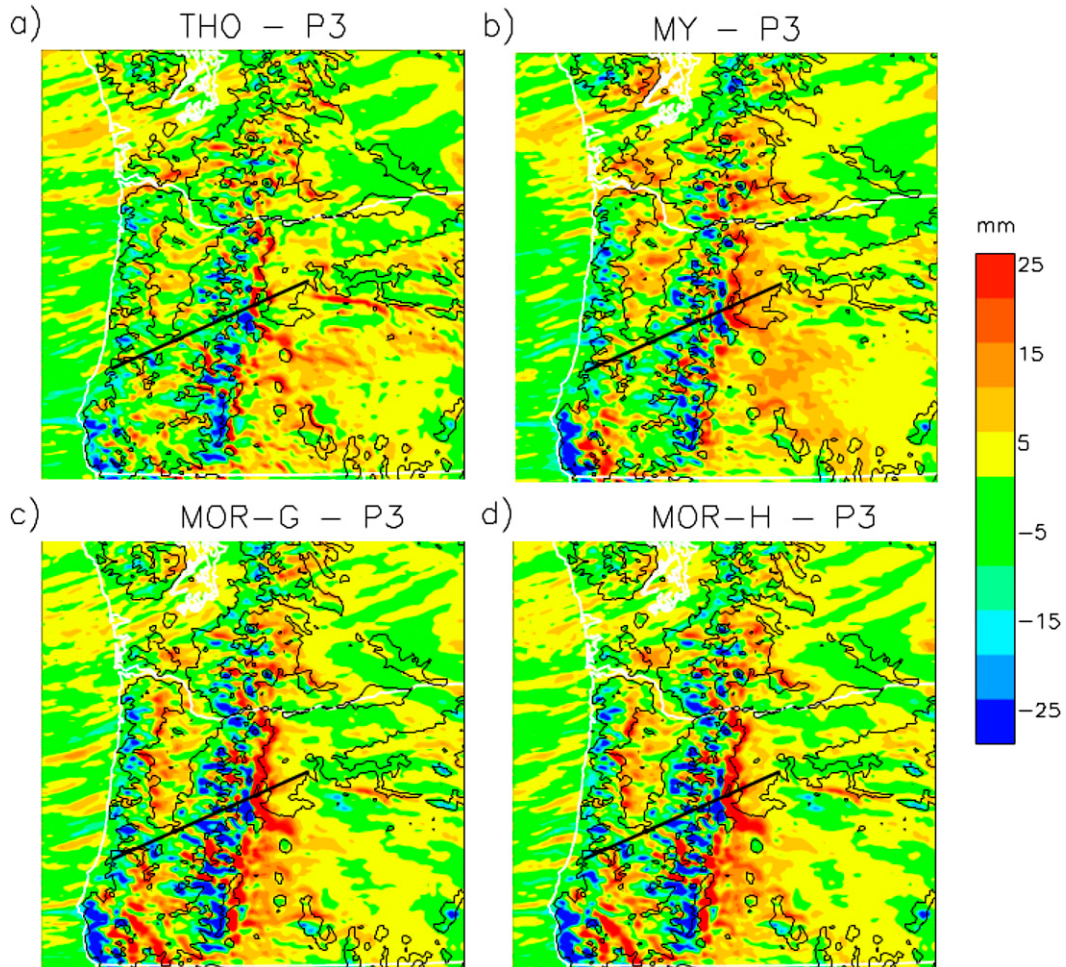
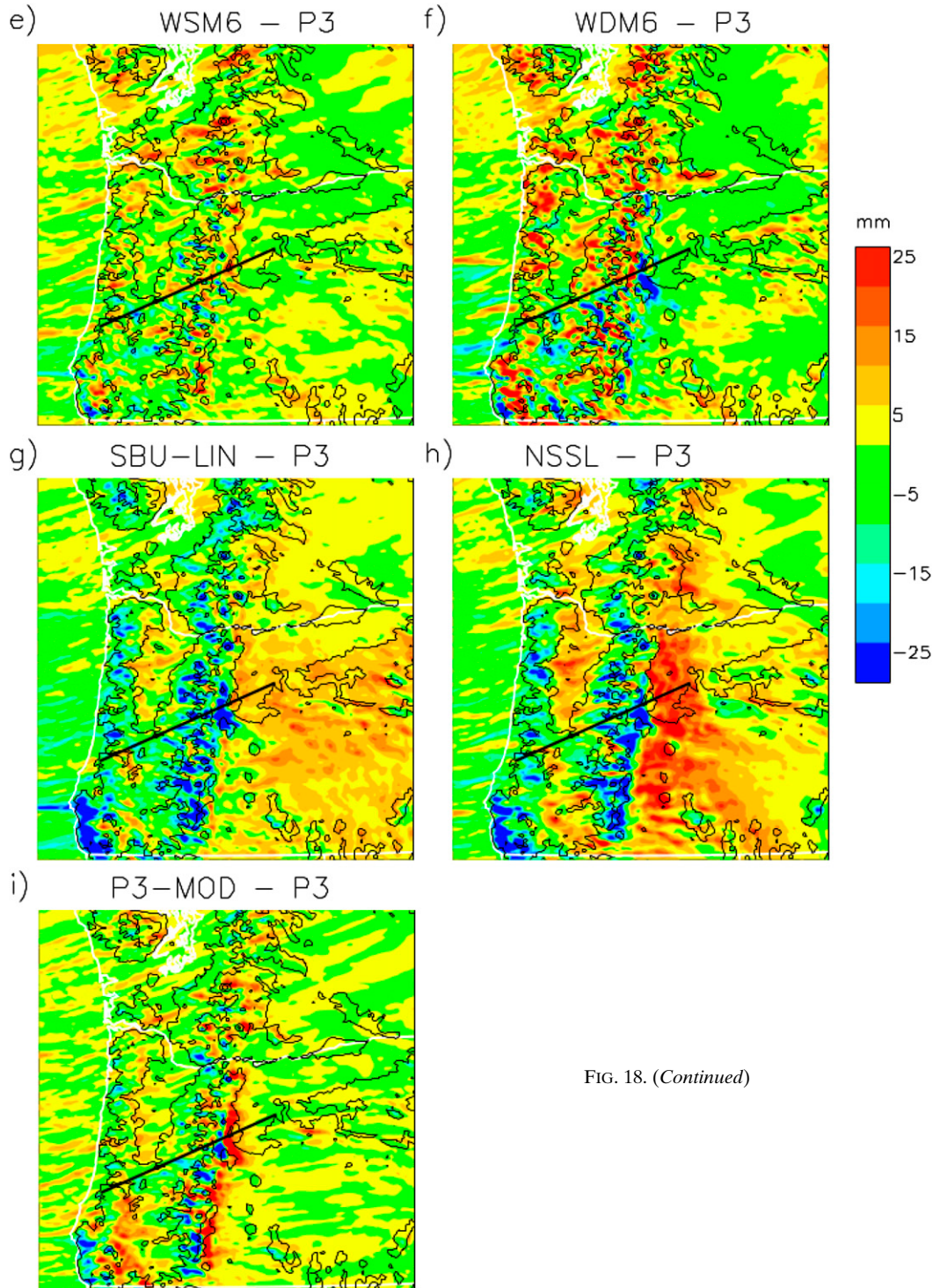


FIG. 18. Difference in accumulated surface precipitation from 1400 UTC 13 Dec to 0800 14 Dec relative to the P3 simulation for (a) THO, (b) MY2, (c) MOR-G, (d) MOR-H, (e) WSM6, (f) WDM6, (g) SBU-LIN, (h) NSSL, and (i) P3-MOD. The thick black line shows the location of the southwest–northeast Convair transect. Thin black contour lines show surface elevation with an interval of 800 m starting at 200 m MSL.

are evident. Six of the schemes (MOR-H, MOR-G, MY2, THO, NSSL, and SBU-LIN) tend to produce greater precipitation in the lee but less on the windward side of major ridges, with THO and SBU-LIN producing less of a difference relative to P3 than MOR-H, MOR-G, MY2, or NSSL. This is seen most clearly along and just east of the Oregon Cascades and, to a lesser extent, along the Coast Range and Willamette Valley. On the other hand, P3 produces a similar distribution of precipitation as WSM6 but more precipitation on the leeward side and less on the windward side of the Cascade and Coast Ranges compared to WDM6. MOR-H, MOR-G, MY2, THO, and SBU-LIN also produce a peak surface precipitation rate along the Convair cross section that is about 6–12 km downwind of the crest, while the peak precipitation rate is anchored near the crest for P3, NSSL, WSM6, and WDM6 (Fig. 19). These

results are generally reflected in the statistical comparison with the seven surface stations in the immediate lee of the Oregon Cascades (see Table 1). While all schemes overpredict leeward precipitation relative to these stations, MOR-G, MOR-H, and MY2 have the greatest bias (factor of 2.5–3 larger than observed) and WDM6 has the smallest (20% larger than observed).

An explanation for the reduced leeward but increased windward precipitation for P3 compared to MOR-G, MOR-H, THO, and NSSL is the greater overall ice fall speed in P3 with its prediction of rime mass fraction and the associated increase in fall speed. While SBU-LIN parameterizes rimed ice using a single category and also includes a diagnostic increase in fall speed in conditions with riming (see appendix), giving  $V_m \sim 2\text{--}3 \text{ m s}^{-1}$  in regions with substantial riming, outside of these regions,  $V_m$  is about one-half that of P3. This difference stems in

FIG. 18. (*Continued*)

part from neglect of the air-density correction factor on particle fall speeds in SBU-LIN. Nonetheless, the increase in fall speed associated with rimed snow in SBU-LIN probably explains why the distribution of surface precipitation is more similar to P3 than most of the other

schemes that do not explicitly represent the increase in fall speed associated with rimed snow. On the other hand, MOR-G, MOR-H, THO, and NSSL predict little graupel mass relative to snow (Table 2). Thus, they generally have a small combined snow-graupel

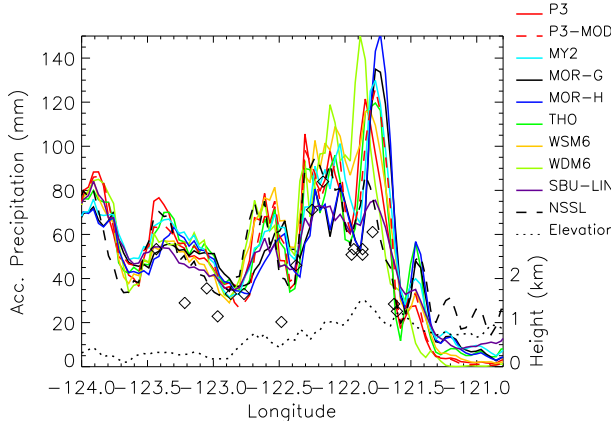


FIG. 19. Accumulated surface precipitation from 1400 UTC 13 Dec to 0800 UTC 14 Dec along the southwest–northeast Convair transect for all simulations. Station observations in the vicinity of the transect are shown by black diamonds, with surface elevation shown by the dotted black line. The location of the transect is shown by the thick black line in Fig. 18.

mass-weighted fall speed,  $V_{sg} = (q_s V_s + q_g V_g)/(q_s + q_g)$ , where  $V_s$  and  $q_s$  and  $V_g$  and  $q_g$  are the fall speeds and mass mixing ratios of snow and graupel, respectively. For example, MOR-G has a peak  $V_{sg}$  of about  $1.5 \text{ m s}^{-1}$  along the southwest–northeast Convair transect above the freezing level, while in NSSL the  $V_{sg}$  is less than  $1.2 \text{ m s}^{-1}$  nearly everywhere above the freezing level. Note that THO includes an ad hoc boost to the mass-weighted mean snowfall speed in conditions with significant riming,<sup>2</sup> as well as below the freezing level to account for partially melted snow. This results in a substantial increase in  $V_{sg}$  below about 750 hPa to values greater than  $2\text{--}3 \text{ m s}^{-1}$  and may explain why THO produces less leeward precipitation than MOR-G, MOR-H, and NSSL and less of a difference relative to P3.

The importance of ice fall speeds on the distribution of surface precipitation is further illustrated by a sensitivity test with P3 but with the number- and mass-weighted fall speeds calculated assuming all ice is unrimed (P3-MOD). This test results in mass-weighted fall speeds that are less than about  $1.7 \text{ m s}^{-1}$  everywhere and a spatial pattern of surface precipitation that is remarkably similar to MOR-G and MOR-H and, to a lesser extent, THO (cf. Fig. 18g with Figs. 18a,c,d).

<sup>2</sup>The ad hoc fall-speed increase associated with riming in THO is applied when the riming rate exceeds the vapor deposition growth rate by a factor of 5. It is given by a multiplicative enhancement factor  $\text{EF} = 1.1 + 0.016(F^* - 5)$ , where  $F^*$  is the ratio of the riming and vapor depositional growth rates and has an allowed maximum value of 30. The fall speed enhancement factor has a maximum allowed value of 1.5.

TABLE 2. Modeled average cloud ice water content (CIWC), snow water content (SWC), and graupel water content (GWC), all in units of grams per cubic meters. Since P3 and P3-MOD do not include separate categories for ice species, the total mean ice water content in these simulations is shown in the column for SWC. Averaging is done along the southwest–northeast Convair flight track (dashed line in Fig. 14b) from 2300 UTC 13 Dec to 0100 UTC 14 Dec and includes all vertical levels.

	CIWC	SWC	GWC
P3	—	0.240	—
MY2	0.039	0.226	0.096
MOR-G	0.008	0.276	0.011
MOR-H	0.008	0.300	0.001
NSSL	0.013	0.434	0.024
SBU-LIN	0.001	0.377	—
THO	0.0001	0.359	0.003
WSM6	0.023	0.176	0.062
WDM6	0.025	0.133	0.075
P3-MOD	—	0.253	—

P3-MOD also gives larger bias and RMSE relative to the observations than P3 for all station subsets (see Table 1).

WSM6 and WDM6 produce large graupel mass contents relative to snow (Table 2) and, hence, large  $V_{sg}$  compared to MOR-G, MOR-H, and THO and less leeward but greater windward precipitation.<sup>3</sup> This is consistent with the results of Lin and Colle (2009), who simulated a different orographic precipitation event from IMPROVE-2. However, MY2 also simulates large amounts of graupel yet gives a spatial distribution of precipitation similar to MOR-H, MOR-G, and THO, with relatively large leeward and small windward precipitation rates. This is surprising since it produces a distribution of  $V_{sg}$  similar to WSM6 and WDM6 and larger than in MOR-G and MOR-H (not shown). Specific reasons for this behavior are unclear but we note that the parameterization of several snow and graupel processes such as vapor deposition and sublimation in MY2 differ from the other schemes. Overall these results suggest that while ice particle fall speed is a key factor contributing to the differences in the spatial distribution of precipitation among schemes, other processes are also important.

Finally, we compare average modeled and observed ice water content (IWC) for the three approximately level southwest–northeast Convair legs (Table 3) and cloud liquid water content (LWC) for the five north–south P-3 flight legs (Table 4). Following Garvert et al.

<sup>3</sup>WSM6 and WDM6 apply the same  $V_{sg}$  to both graupel and snow in their codes. However, a sensitivity test with the mass-weighted snow and graupel fall speeds applied separately to snow and graupel in WSM6 produced little difference in the spatial distribution of precipitation.

TABLE 3. Modeled and observed average IWC ( $\text{g m}^{-3}$ ) for the three approximately level southwest–northeast Convair flight legs (red dotted lines in Fig. 15b). The geographic location of the transect is shown by the dashed line in Fig. 14b. Approximate pressure level of the legs is given in the first row. Modeled IWC is the sum of cloud ice, snow, and graupel for the schemes that include these as separate species and is an average from 2300 UTC 13 Dec to 0100 UTC 14 Dec.

	Leg 1 (470 hPa)	Leg 2 (515 hPa)	Leg 3 (550 hPa)
Obs	0.12	0.16	0.25
P3	0.40	0.47	0.54
MY2	0.62	0.79	0.90
MOR-G	0.40	0.51	0.60
MOR-H	0.47	0.55	0.64
NSSL	1.21	1.14	1.05
SBU-LIN	0.77	0.85	0.85
THO	0.65	0.72	0.78
WSM6	0.43	0.53	0.60
WDM6	0.43	0.50	0.57
P3-MOD	0.39	0.45	0.56

(2005b), the modeled values are time averages around the approximate time of the flights (2300 UTC 13 December–0100 UTC 14 December). While this comparison illustrates systematic differences between model results and observations, we note that the in situ aircraft measurements are of limited spatial extent. Here the modeled IWC is the sum of all ice categories for the schemes that include separate categories. Similar to results of Garvert et al. (2005a,b) and Milbrandt et al. (2008), there is an overprediction of IWC for all simulations. However, P3 produces less ice aloft than the other schemes, especially compared to THO, MY2, SBU-LIN, and NSSL. This may partly result from differences in ice particle fall speeds discussed above. This was also suggested by Lin and Colle (2011), who simulated this case and another one from IMPROVE-2 using the SBU-LIN and MOR-G schemes and two versions of the THO scheme. However, they also found that

SBU-LIN reduced the ice content aloft compared with the other schemes, which contrasts with our results. Specific reasons for these differences are unclear, but they might be explained by differences in the model setup or more recent changes to the MOR-G and THO schemes. The relationship between IWC aloft and surface precipitation is less clear when comparing all schemes here, presumably because there are several aspects besides particle fall speeds that differ between schemes.

There is also a fairly large spread of supercooled LWC (including cloud water and rain) among simulations for the P-3 flight legs, in some instances exceeding  $0.3 \text{ g m}^{-3}$  (Table 4). WDM6 produces relatively little liquid water, while MOR-G, MOR-H, and MY2 produce much larger LWC. SBU-LIN produces substantially larger LWC than the other schemes, especially near and downwind of the Cascades' crest, which is consistent with the results of Lin and Colle (2011). In general, schemes reasonably predict LWC on the windward slope compared to the aircraft observations (except for underprediction by WDM6), while all schemes underpredict LWC by  $0.01\text{--}0.1 \text{ g m}^{-3}$  over the crest except SBU-LIN, which overpredicts LWC. This common spatial pattern of bias, with the exception of SBU-LIN, may also reflect other aspects of the model besides microphysics, such as the inability of 3-km horizontal grid spacing to resolve detailed orography that is expected to impact flow over the crest [although we note that Lin and Colle (2011) found a similar underprediction of LWC for MOR-G and THO using WRF with 1.33-km horizontal grid spacing].

## 6. Computational efficiency tests

An important aspect of any physical parameterization in an atmospheric model is the computational cost. Microphysics schemes add cost due to the microphysical process calculations themselves as well as advection and

TABLE 4. Modeled and observed average cloud LWC ( $\text{g m}^{-3}$ ) for the five north–south P-3 flight legs (solid black lines in Fig. 14b), with numbering starting from the westernmost leg. Approximate pressure level of the legs is given in the first row. Modeled values are averaged from 2300 UTC 13 Dec to 0100 UTC 14 Dec.

	Leg 1 (775 hPa)	Leg 2 (725 hPa)	Leg 3 (650 hPa)	Leg 4 (600 hPa)	Leg 5 (675 hPa)
Obs	0.14	0.26	0.20	0.12	0.04
P3	0.26	0.09	0.03	0.02	0.01
MY2	0.34	0.25	0.18	0.09	0.01
MOR-G	0.37	0.20	0.14	0.07	0.01
MOR-H	0.39	0.20	0.14	0.08	0.01
NSSL	0.35	0.23	0.09	0.06	0.00
SBU-LIN	0.34	0.58	0.68	0.51	0.11
THO	0.28	0.08	0.04	0.03	0.01
WSM6	0.22	0.15	0.05	0.02	0.01
WDM6	0.01	0.11	0.06	0.03	0.02
P3-MOD	0.29	0.07	0.03	0.02	0.01

TABLE 5. Timing results for the squall-line and orographic simulations. Presented values are average wall-clock time per model time step (s), excluding time steps that write to output or restart files. Times relative to those of WSM6 are indicated parenthetically. The number of prognostic hydrometeor variables in each scheme is also shown in the rightmost column. Results for MOR-G are nearly the same as MOR-H and therefore not shown.

	Squall-line case	Orographic case	Number of prognostic variables
P3	0.236 (1.113)	0.718 (1.061)	7
MY2	0.301 (1.420)	1.012 (1.495)	12
MOR-H	0.256 (1.203)	0.813 (1.200)	9
NSSL	0.334 (1.575)	1.004 (1.483)	13
SBU-LIN	0.215 (1.014)	0.712 (1.052)	4
THO	0.257 (1.212)	0.795 (1.174)	7
WSM6	0.212 (1.000)	0.677 (1.000)	5
WDM6	0.251 (1.184)	0.777 (1.148)	8

diffusion of the prognostic microphysical variables. To assess the cost of P3 compared to other schemes, timing tests were conducted on all simulations for both cases. The model runs were performed using 256 and 720 processors on the NCAR Yellowstone supercomputer (<http://n2t.net/ark:/85065/d7wd3xhc>) with the Intel compiler for the squall-line and orographic cases, respectively. The total wall clock time per time step was analyzed, excluding steps writing to output or restart files. For the squall line, the run time was averaged between 3 and 7 h, when the squall line is in a quasi-steady mature phase. For the orographic case the run time was averaged between 1200 UTC 13 December and 1200 UTC 14 December (hours 12–36 of the forecast).

The timing results are summarized in Table 5. Differences in run time primarily reflect the number of prognostic variables included in the schemes and the associated with the cost of advection (and mixing). In general, in WRF, there is an increase of several percent in total run time per added prognostic variable. However, there are also differences in cost associated with the microphysical process calculations between the schemes. For example, P3 and THO have the same number of prognostic variables (seven) but the simulations with P3 are 8.2% and 9.7% faster for squall line and orographic cases, respectively. The runs with P3 are only somewhat slower than the WSM6 scheme (11.3% and 6.1% for the squall line and orographic cases, respectively), despite its inclusion of two more prognostic variables. This reflects efforts to optimize the code and the efficiency of the lookup table approach described in Part I.

## 7. Summary and conclusions

In this study, the new P3 microphysics scheme introduced in Part I was tested in high-resolution WRF simulations for two contrasting, well-observed case

studies. Results were compared with observations and with simulations using several other schemes available in WRF. For the squall-line case, the simulation with P3 exhibited reasonable reflectivity and precipitation structures compared to the observed squall line. In particular, it produced a narrow leading edge of high reflectivity associated with convective precipitation and a wide trailing stratiform region that several of the schemes were unable to simulate. Despite the use of a single ice category, P3 predicted a wide range of ice particle characteristics in different parts of the squall line. Simulations with the various schemes as well as additional sensitivity tests suggested that the representation of rimed-ice fall speed was critical for squall-line structure, which is consistent with previous studies (Bryan and Morrison 2012; Adams-Selin et al. 2013). In particular, the representation of rimed ice as hail in MOR-H, the occurrence of substantial hail and dense graupel in NSSL, and the prediction of ice with hail-like characteristics in the convective region in P3 led to a well-defined leading convective region with high precipitation rates that matched well with observations. In contrast, schemes that represent rimed ice as slower-falling graupel had less defined convective regions with lower peak precipitation rates. All schemes underpredicted precipitation rates in the rearward part of the trailing stratiform region. Schemes also struggled to simulate correctly the observed and retrieved raindrop median volume diameter. These results suggest uncertainty in the correct representation of rain microphysics in all of the two-moment schemes.

For the orographic precipitation case, the dynamical forcing was largely constrained by the synoptic-scale flow and orographic enhancement, while microphysical–dynamical feedbacks played a larger role in the squall-line case. Nonetheless, there were notable differences in the distribution of surface precipitation among simulations for the orographic case. P3 was able to represent the increase in fall speed associated with lightly or moderately rimed snow and, hence, produced greater windward and less leeward precipitation compared to most of the other schemes. A similar result occurred with SBU-LIN, which treats the increased fall speed for rimed snow using a diagnostic riming intensity factor. However, the overall fall speed in regions without riming in SBU-LIN was about one-half that of P3 and it also produced less windward and greater leeward precipitation than P3, although to a lesser degree than many other schemes. A sensitivity test with fall speed calculated assuming unrimed snow in P3 produced a distribution of surface precipitation similar to that of several of the schemes that predicted large amounts of snow relative to graupel and, therefore, had similarly low fall

speeds. The importance of riming and particle fall speeds on the distribution of orographic precipitation is consistent with several previous studies ([Colle and Mass 2000; Colle and Zeng 2004; Garvert et al. 2005b; Lin and Colle 2009; Lin and Colle 2011](#)).

It was argued in [Part I](#) that parameterizing ice-phase microphysical processes by predicting bulk particle properties for a single free ice-phase category in P3, rather than partitioning ice into predefined categories, has several conceptual advantages. The real-case simulations examined in this study, with comparisons to microphysics schemes using the traditional predefined ice-phase category approach, suggest that the P3 scheme is also viable in terms of practical performance. Furthermore, P3 is computationally efficient. It must be emphasized, however, that the scheme must be tested on many more cases covering a wide range of conditions. Moreover, other aspects such as cloud cover and radiative fluxes should be investigated and compared with observations. Such efforts will be a focus of future work, as well as further development efforts for P3 discussed in [Part I](#), including multiple free-ice categories that each can evolve to any ice type. We also anticipate using the predicted particle properties directly in instrument simulators (e.g., polarimetric radar) as an additional method for evaluation.

**Acknowledgments.** This work was partially supported by the U.S. DOE ASR DE-SC0008648, U.S. DOE ASR DE-SC0005336, sub-awarded through NASA NNX12AH90G, and the NSF Science and Technology Center for Multiscale Modeling of Atmospheric Processes (CMMAP), managed by Colorado State University under Cooperative Agreement ATM-0425247. We thank W. Grabowski, D. Dawson, and M. Kumjian for valuable discussion, E. Brandes for collecting and analyzing the Oklahoma disdrometer observations, and M. Stoelinga, B. Colle, M. Garvert, and others involved in the IMPROVE-2 project for collecting the measurements used in this study. We thank T. Mansell for comments on the manuscript and help in use of the NSSL scheme and Y. Lin for help with the SBU-LIN scheme. We also acknowledge high-performance computing support from Yellowstone provided by NCAR's Computational and Information Systems Laboratory, sponsored by the National Science Foundation.

## APPENDIX

### Overview of the Microphysics Schemes

A complete description of the predicted particle properties (P3) scheme is given in [Part I](#). The other

microphysics schemes tested are briefly described below.

#### a. Milbrandt–Yau two moment (MY2)

The multimoment Milbrandt–Yau scheme is described in [Milbrandt and Yau \(2005a,b\)](#) and references therein, with modifications discussed in [Milbrandt et al. \(2010\)](#) and [Milbrandt et al. \(2012\)](#). The scheme has prognostic equations for moments of six hydrometeor categories: cloud (liquid droplets), rain (precipitating drops), ice (pristine crystals), snow (large crystals/aggregates), graupel (rimed ice), and hail (high-density rimed ice and/or frozen drops), where the particle size distribution (PSD) of each category  $x$  is represented by a complete gamma function (of the same form as used in P3; see [Part I](#)). In this study, the standard two-moment (with prognostic mixing ratios  $q_x$  and total number mixing ratios  $N_x$ ) fixed- $\mu_x$  version (MY2) is used, with  $\mu_x = 0$  for  $x = i, r, s, g, h$  and  $\mu_x = 3$  for cloud droplets. All particles except for snow are assumed to be spherical with constant bulk densities  $\rho_x$ . Thus, for the standard mass–diameter relation  $m(D) = c_x D^{dx}$ , each category  $c_x = (\pi/6)\rho_x$  and  $d_x = 3$ , where  $D$  is the maximum dimension (or diameter) of the particle. The snow category uses  $c_s = 0.1597$  and  $d_s = 2.078$  (mks units). This implies a variable bulk snow density, which varies inversely with the mean size. For ice, graupel, and hail, fixed bulk densities of 100, 400, and  $900 \text{ kg m}^{-3}$ , respectively, are used.

A modified version of the scheme (available in WRF, version 3.6, but not WRF, version 3.4.1, which was used in this study) addresses several of the biases evident in the squall-line simulation with MY2 described in [section 4b](#). The conversion of cloud ice to snow is now parameterized by converting the portion of the ice size distribution with sizes greater than  $125 \mu\text{m}$ ; this results in an improved stratiform rain region for the squall-line case described in [section 4b](#). Similarly, the conversion of graupel to hail has been modified and now considers the portion of the graupel size distribution greater than the size defined by the Schumann–Ludlam limit ([Milbrandt and Yau 2005b](#)); if this concentration exceeds a threshold value of  $0.01 \text{ m}^{-3}$ , then this tail portion of the graupel distribution is converted to hail. Furthermore, the standard MY2 scheme has a minimum mean-mass hail diameter of 5 mm, which frequently results in hail being excessively reclassified as graupel; this value has been reduced to 1 mm, which leads to larger hail contents simulated in convective regions.

#### b. Morrison (MOR-H and MOR-G)

The Morrison two-moment microphysics scheme ([Morrison et al. 2005, 2009; Morrison and Milbrandt 2011](#))

prognoses mass and number mixing ratios of rain, cloud ice, snow, and graupel/hail and mass mixing ratio of cloud droplets. There is a user-set switch for the rimed-ice category to have properties consistent with graupel (MOR-G) or hail (MOR-H). MOR-G and MOR-H differ in the bulk density and fall speed-size relationship for rimed ice. Given previous studies documenting the importance of rimed ice characteristics, especially fall speed in deep convective systems (Morrison and Milbrandt 2011; Bryan and Morrison 2012; Van Weverberg 2013; Adams-Selin 2013), both MOR-G and MOR-H are tested here. All species except cloud droplets are assumed to follow inverse-exponential size distributions. The cloud droplet size distribution follows a gamma function with a spectral dispersion parameterized following observations of Martin et al. (1994). Ice particles are assumed to be spherical with bulk densities of 500, 100, 400, and  $900 \text{ kg m}^{-3}$  for cloud ice, snow, graupel, and hail, respectively.

#### *c. NOAA/National Severe Storms Laboratory (NSSL)*

The NSSL scheme is an extension of the original two-moment scheme of Ziegler (1985) and is described in Mansell et al. (2010) and Mansell (2010). It prognoses number and mass mixing ratios of cloud droplets, rain, small ice, snow, graupel, and hail, as well as the particle volume of graupel allowing for prediction of graupel density (Mansell et al. 2010). The default settings of the scheme are used, which employ inverse-exponential size distributions for rain, and graupel, and a gamma distribution with shape parameter  $\mu = 1$  for hail. Cloud ice and snow are represented by mass distributions; for cloud ice, the distribution is assumed to be inverse exponential and for snow the assumed shape parameter is  $-0.8$ . Snow and hail particles are assumed spherical with bulk densities of 100 and  $900 \text{ kg m}^{-3}$ , respectively.

#### *d. Stony Brook University–Lin (SBU-LIN)*

The scheme of Lin and Colle (2011) is a one-moment scheme that prognoses mass mixing ratios of cloud droplets, rain, cloud ice, and precipitating ice. It uses a diagnostic method to determine the properties of precipitating ice (snow and graupel) as a function of particle habit (assumed to be a function of local temperature) and riming. The latter is calculated through a nondimensional riming intensity parameter ( $R_i$ ) that is equal to the ratio of the riming growth rate to the riming plus depositional growth rates. The mass-size and projected area-size relationships for conditions with  $R_i = 0$  are a function of temperature following Heymsfield et al. (2007), and these are modified when  $R_i > 0$  to account for increasing roundness and density of particles

during riming. Ice particle fall speed is calculated from the mass-size and projected area-size relationships using the Best number approach of Mitchell (1996). Rain and precipitating ice particle size distributions are assumed to be inverse-exponential shape. The  $N_0$  value for precipitating ice follows that of WSM6. Autoconversion of cloud droplets to rain follows Liu and Daum (2004), while most other processes follow Lin et al. (1983).

#### *e. Thompson (THO)*

The Thompson et al. (2008) microphysics scheme prognoses the mass mixing ratios of cloud droplets, cloud ice, rain, snow, and a hybrid graupel–hail category, plus the number mixing ratios of cloud ice and rain. Snow is unique in this scheme because its density varies inversely with diameter and its size distribution is a sum of two gamma functions following observations by Field et al. (2005); most other WRF bulk schemes assume constant-density snow and inverse-exponential size distributions. The remaining species all follow a generalized gamma distribution with  $\mu = 0$  for cloud ice, rain, and graupel but a variable shape parameter for cloud water following observations of Martin et al. (1994), similar to the Morrison scheme. The graupel–hail hybrid category has a two-parameter diagnostic dependence of its size distribution intercept parameter based on the mass mixing ratio and amount of supercooled liquid water coincident in a grid volume. Other unique aspects of this scheme include an increase to snow terminal velocity due to heavy riming of cloud water and increased terminal velocity of snow and graupel during melting. This scheme has recently been shown to realistically predict upper-level ice clouds (Cintineo et al. 2014; Jin et al. 2014) compared to satellite data and against other bulk schemes. This scheme and the Morrison et al. (2009) scheme outperformed other bulk schemes tested for seasonal snowfall prediction in the Colorado Rockies (Liu et al. 2011).

#### *f. WRF single moment (WSM6)*

The WSM6 scheme is one moment and prognoses mass mixing ratios for five hydrometeor categories: cloud droplets, rain, cloud ice, snow, and graupel (Hong et al. 2004; Hong and Lim 2006). It assumes inverse-exponential size distributions for rain, snow, and graupel. It specifies constant values of intercept parameter  $N_0$  of  $8 \times 10^6$  and  $4 \times 10^6 \text{ m}^{-4}$  for rain and graupel, respectively. For snow,  $N_0$  is a function of temperature following Houze et al. (1979), with an upper bound set to  $2 \times 10^8 \text{ m}^{-4}$ . The cloud ice crystal concentration is diagnosed as a function of cloud ice mass mixing ratio. Snow and graupel particles are assumed to be spherical with bulk densities of 100 and  $400 \text{ kg m}^{-3}$ , respectively.

Microphysical process calculations generally follow Rutledge and Hobbs (1983) and Dudhia (1989), except that autoconversion of cloud water to rain follows Tripoli and Cotton (1980).

#### *g. WRF double moment (WDM6)*

The WDM6 scheme prognoses mass mixing ratios of cloud droplets, rain, cloud ice, snow, and graupel and number mixing ratios of cloud droplets, rain, and cloud condensation nuclei (Lim and Hong 2010). The cloud droplet and rain size distributions are assumed to follow generalized four-parameter gamma functions, with the two dispersion parameters specified as constants and the slope and intercept parameters diagnosed from the prognosed mass and number mixing ratios and specified dispersion parameters. For rain, the dispersion parameter settings are such that the size distribution is equivalent to a three-parameter gamma function with  $\mu = 1$ , similar to the other schemes except that  $\mu$  for rain is allowed to vary between 0 and 8.28 in P3 while  $\mu = 0$  for MY2, THO, WSM6, MOR-G, and MOR-H. The two-moment scheme for droplet collision-coalescence (autoconversion and accretion) follows from Cohard and Pinty (2000). Ice processes follow WSM6.

#### REFERENCES

- Adams-Selin, R. D., S. C. van den Heever, and R. H. Johnson, 2013: Impact of graupel parameterization schemes on idealized bow echo simulations. *Mon. Wea. Rev.*, **141**, 1241–1262, doi:[10.1175/MWR-D-12-00064.1](https://doi.org/10.1175/MWR-D-12-00064.1).
- Barlage, M., and Coauthors, 2010: Noah land surface modifications to improve snowpack prediction in the Colorado Rocky Mountains. *J. Geophys. Res.*, **115**, D22101, doi:[10.1029/2009JD013470](https://doi.org/10.1029/2009JD013470).
- Biggerstaff, M. I., and R. A. Houze, 1991: Kinematic and precipitation structure of the 10–11 June 1985 squall line. *Mon. Wea. Rev.*, **119**, 3034–3065, doi:[10.1175/1520-0493\(1991\)119<3034:KAPSOT>2.0.CO;2](https://doi.org/10.1175/1520-0493(1991)119<3034:KAPSOT>2.0.CO;2).
- , and —, 1993: Kinematics and microphysics of the transition zone of the 10–11 June 1985 squall line. *J. Atmos. Sci.*, **50**, 3091–3110, doi:[10.1175/1520-0469\(1993\)050<3091:KAMOTT>2.0.CO;2](https://doi.org/10.1175/1520-0469(1993)050<3091:KAMOTT>2.0.CO;2).
- Braun, S. A., and R. A. Houze, 1994: The transition zone and secondary maximum of radar reflectivity behind a midlatitude squall line: Results retrieved from Doppler radar data. *J. Atmos. Sci.*, **51**, 2733–2755, doi:[10.1175/1520-0469\(1994\)051<2733:TTZASM>2.0.CO;2](https://doi.org/10.1175/1520-0469(1994)051<2733:TTZASM>2.0.CO;2).
- Bryan, G. H., and H. Morrison, 2012: Sensitivity of a simulated squall line to horizontal resolution and parameterization of microphysics. *Mon. Wea. Rev.*, **140**, 202–225, doi:[10.1175/MWR-D-11-00046.1](https://doi.org/10.1175/MWR-D-11-00046.1).
- , J. C. Knievel, and M. D. Parker, 2006: A multimodel assessment of RKW theory's relevance to squall-line characteristics. *Mon. Wea. Rev.*, **134**, 2772–2792, doi:[10.1175/MWR3226.1](https://doi.org/10.1175/MWR3226.1).
- Cintineo, R., J. A. Otkin, M. Xue, and F. Kong, 2014: Evaluating the performance of planetary boundary layer and cloud microphysical parameterization schemes in convection-permitting ensemble forecasts using synthetic GOES-13 satellite observations. *Mon. Wea. Rev.*, **142**, 163–182, doi:[10.1175/MWR-D-13-00143.1](https://doi.org/10.1175/MWR-D-13-00143.1).
- Clark, A. J., and Coauthors, 2012: An overview of the 2010 Hazardous Weather Testbed Experimental Forecast Program Spring Experiment. *Bull. Amer. Meteor. Soc.*, **93**, 55–74, doi:[10.1175/BAMS-D-11-00040.1](https://doi.org/10.1175/BAMS-D-11-00040.1).
- Cohard, J.-M., and J.-P. Pinty, 2000: A comprehensive two-moment warm microphysical bulk scheme. I: Description and tests. *Quart. J. Roy. Meteor. Soc.*, **126**, 1815–1842, doi:[10.1256/smsqj.56613](https://doi.org/10.1256/smsqj.56613).
- Colle, B. A., and C. F. Mass, 2000: The 5–9 February 1996 flooding event over the Pacific Northwest: Sensitivity studies and evaluation of the MM5 precipitation forecasts. *Mon. Wea. Rev.*, **128**, 593–617, doi:[10.1175/1520-0493\(2000\)128<0593:TFFEOT>2.0.CO;2](https://doi.org/10.1175/1520-0493(2000)128<0593:TFFEOT>2.0.CO;2).
- , and Y. Zeng, 2004: Bulk microphysical sensitivities within the MM5 for orographic precipitation. Part I: The Sierra 1986 event. *Mon. Wea. Rev.*, **132**, 2780–2801, doi:[10.1175/MWR2821.1](https://doi.org/10.1175/MWR2821.1).
- , M. F. Garvert, J. B. Wolfe, C. F. Mass, and C. P. Woods, 2005: The 13–14 December 2001 IMPROVE-2 event. Part III: Simulated microphysical budgets and sensitivity studies. *J. Atmos. Sci.*, **62**, 3535–3558, doi:[10.1175/JAS3552.1](https://doi.org/10.1175/JAS3552.1).
- Dudhia, J., 1989: Numerical study of convection observed during the Winter Monsoon Experiment using a mesoscale two-dimensional model. *J. Atmos. Sci.*, **46**, 3077–3107, doi:[10.1175/1520-0469\(1989\)046<3077:NSOCOD>2.0.CO;2](https://doi.org/10.1175/1520-0469(1989)046<3077:NSOCOD>2.0.CO;2).
- Field, P. R., R. J. Hogan, P. R. A. Brown, A. J. Illingworth, T. W. Choularton, and R. J. Cotton, 2005: Parametrization of ice-particle size distributions for mid-latitude stratiform cloud. *Quart. J. Roy. Meteor. Soc.*, **131**, 1997–2017, doi:[10.1256/qj.04.134](https://doi.org/10.1256/qj.04.134).
- Garvert, M. F., B. A. Colle, and C. F. Mass, 2005a: The 13–14 December 2001 IMPROVE-2 event. Part I: Synoptic and mesoscale evolution and comparison with a mesoscale model simulation. *J. Atmos. Sci.*, **62**, 1997–2017, doi:[10.1175/JAS3549.1](https://doi.org/10.1175/JAS3549.1).
- , C. P. Woods, B. A. Colle, C. F. Mass, P. V. Hobbs, M. T. Stoelinga, and J. B. Wolfe, 2005b: The 13–14 December 2001 IMPROVE-2 event. Part II: Comparisons of MM5 model simulations of clouds and precipitation with observations. *J. Atmos. Sci.*, **62**, 3520–3534, doi:[10.1175/JAS3551.1](https://doi.org/10.1175/JAS3551.1).
- , B. Smull, and C. Mass, 2007: Multiscale mountain waves influencing a major orographic precipitation event. *J. Atmos. Sci.*, **64**, 711–737, doi:[10.1175/JAS3876.1](https://doi.org/10.1175/JAS3876.1).
- Grabowski, W. W., 2001: Coupling cloud processes with the large-scale dynamics using the cloud-resolving convection parameterization (CRCP). *J. Atmos. Sci.*, **58**, 978–997, doi:[10.1175/1520-0469\(2001\)058<0978:CCPWTL>2.0.CO;2](https://doi.org/10.1175/1520-0469(2001)058<0978:CCPWTL>2.0.CO;2).
- , 2006: Sixth WMO International Cloud Modeling Workshop. *Bull. Amer. Meteor. Soc.*, **87**, 639–642, doi:[10.1175/BAMS-87-5-639](https://doi.org/10.1175/BAMS-87-5-639).
- Heymsfield, A. J., A. Bansemer, and C. W. Twohy, 2007: Refinements to ice particle mass dimensional and terminal velocity relationships for ice clouds. Part I: Temperature dependence. *J. Atmos. Sci.*, **64**, 1047–1067, doi:[10.1175/JAS3890.1](https://doi.org/10.1175/JAS3890.1).
- Hong, S.-Y., and H.-L. Pan, 1996: Nonlocal boundary layer vertical diffusion in a medium-range forecast model. *Mon. Wea. Rev.*, **124**, 2322–2339, doi:[10.1175/1520-0493\(1996\)124<2322:NBLVDI>2.0.CO;2](https://doi.org/10.1175/1520-0493(1996)124<2322:NBLVDI>2.0.CO;2).

- , and J.-O. J. Lim, 2006: The WRF single-moment 6-class microphysics scheme (WSM6). *J. Korean Meteor. Soc.*, **42**, 129–151.
- , J. Dudhia, and S.-H. Chen, 2004: A revised approach to ice microphysical processes for the bulk parameterization of clouds and precipitation. *Mon. Wea. Rev.*, **132**, 103–120, doi:[10.1175/1520-0493\(2004\)132<0103:ARATIM>2.0.CO;2](https://doi.org/10.1175/1520-0493(2004)132<0103:ARATIM>2.0.CO;2).
- , Y. Noh, and J. Dudhia, 2006: A new vertical diffusion package with an explicit treatment of entrainment processes. *Mon. Wea. Rev.*, **134**, 2318–2341, doi:[10.1175/MWR3199.1](https://doi.org/10.1175/MWR3199.1).
- Houze, R. A., Jr., and S. Medina, 2005: Turbulence as a mechanism for orographic precipitation enhancement. *J. Atmos. Sci.*, **62**, 3599–3623, doi:[10.1175/JAS3555.1](https://doi.org/10.1175/JAS3555.1).
- , P. V. Hobbs, P. H. Herzegh, and D. B. Parsons, 1979: Size distributions of precipitation particles in frontal clouds. *J. Atmos. Sci.*, **36**, 156–162, doi:[10.1175/1520-0469\(1979\)036<0156:SDOPPI>2.0.CO;2](https://doi.org/10.1175/1520-0469(1979)036<0156:SDOPPI>2.0.CO;2).
- , M. I. Biggerstaff, S. A. Rutledge, and B. F. Smull, 1989: Interpretation of Doppler weather radar displays of mid-latitude mesoscale convective systems. *Bull. Amer. Meteor. Soc.*, **70**, 608–619, doi:[10.1175/1520-0477\(1989\)070<0608:IODWRD>2.0.CO;2](https://doi.org/10.1175/1520-0477(1989)070<0608:IODWRD>2.0.CO;2).
- Iacono, M. J., J. S. Delamere, E. J. Mlawer, M. W. Shephard, S. A. Clough, and W. D. Collins, 2008: Radiative forcing by long-lived greenhouse gases: Calculations with the AER radiative transfer models. *J. Geophys. Res.*, **113**, D13103, doi:[10.1029/2008JD009944](https://doi.org/10.1029/2008JD009944).
- Jin, Y., and Coauthors, 2014: The impact of ice phase cloud parameterizations on tropical cyclone prediction. *Mon. Wea. Rev.*, **142**, 606–625, doi:[10.1175/MWR-D-13-00058.1](https://doi.org/10.1175/MWR-D-13-00058.1).
- Kain, J. S., and Coauthors, 2008: Some practical considerations regarding horizontal resolution in the first generation of operational convection-allowing NWP. *Wea. Forecasting*, **23**, 931–952, doi:[10.1175/WAF2007106.1](https://doi.org/10.1175/WAF2007106.1).
- Khairoutdinov, M. F., and D. A. Randall, 2001: A cloud resolving model as a cloud parameterization in the NCAR Community Climate System Model: Preliminary results. *Geophys. Res. Lett.*, **28**, 3617–3620, doi:[10.1029/2001GL013552](https://doi.org/10.1029/2001GL013552).
- Kruger, A., and W. F. Krajewski, 2002: Two-dimensional video disdrometer: A description. *J. Atmos. Oceanic Technol.*, **19**, 602–617, doi:[10.1175/1520-0426\(2002\)019<0602:TDVDAD>2.0.CO;2](https://doi.org/10.1175/1520-0426(2002)019<0602:TDVDAD>2.0.CO;2).
- Lang, T. J., W. A. Lyons, S. A. Rutledge, J. D. Meyer, D. R. MacGorman, and S. A. Cummer, 2010: Transient luminous events above two mesoscale convective systems: Storm structure and evolution. *J. Geophys. Res.*, **115**, A00E22, doi:[10.1029/2009JA014500](https://doi.org/10.1029/2009JA014500).
- Lean, H. W., P. A. Clark, M. Dixon, N. M. Roberts, A. Fitch, R. Forbes, and C. Halliwell, 2008: Characteristics of high-resolution versions of the Met Office Unified Model for forecasting convection over the United Kingdom. *Mon. Wea. Rev.*, **136**, 3408–3424, doi:[10.1175/2008MWR2332.1](https://doi.org/10.1175/2008MWR2332.1).
- Lebo, Z. J., and H. Morrison, 2014: Dynamical effects of aerosol perturbations on simulated idealized squall lines. *Mon. Wea. Rev.*, **142**, 991–1009, doi:[10.1175/MWR-D-13-00156.1](https://doi.org/10.1175/MWR-D-13-00156.1).
- Lim, K.-S. S., and S.-Y. Hong, 2010: Development of an effective double-moment cloud microphysics scheme with prognostic cloud condensation nuclei (CCN) for weather and climate models. *Mon. Wea. Rev.*, **138**, 1587–1612, doi:[10.1175/2009MWR2968.1](https://doi.org/10.1175/2009MWR2968.1).
- Lin, Y., and B. A. Colle, 2009: The 4–5 December 2001 IMPROVE-2 event: Observed microphysics and comparisons with the Weather Research and Forecasting model. *Mon. Wea. Rev.*, **137**, 1372–1392, doi:[10.1175/2008MWR2653.1](https://doi.org/10.1175/2008MWR2653.1).
- , and —, 2011: A new bulk microphysical scheme that includes riming intensity and temperature-dependent ice characteristics. *Mon. Wea. Rev.*, **139**, 1013–1035, doi:[10.1175/2010MWR3293.1](https://doi.org/10.1175/2010MWR3293.1).
- Lin, Y.-L., R. Farley, and H. D. Orville, 1983: Bulk parameterization of the snow field in a cloud model. *J. Climate Appl. Meteor.*, **22**, 1065–1092, doi:[10.1175/1520-0450\(1983\)022<1065:BPOTSF>2.0.CO;2](https://doi.org/10.1175/1520-0450(1983)022<1065:BPOTSF>2.0.CO;2).
- Liu, C., K. Ikeda, G. Thompson, R. Rasmussen, and J. Dudhia, 2011: High-resolution simulations of wintertime precipitation in the Colorado Headwaters region: Sensitivity to physics parameterizations. *Mon. Wea. Rev.*, **139**, 3533–3553, doi:[10.1175/MWR-D-11-00009.1](https://doi.org/10.1175/MWR-D-11-00009.1).
- Liu, Y., and P. H. Daum, 2004: Parameterization of the auto-conversion process. Part I: Analytic formulation of the Kessler-type parameterizations. *J. Atmos. Sci.*, **61**, 1539–1548, doi:[10.1175/1520-0469\(2004\)061<1539:POTAPI>2.0.CO;2](https://doi.org/10.1175/1520-0469(2004)061<1539:POTAPI>2.0.CO;2).
- Luo, Y., Y. Wang, H. Wang, Y. Zheng, and H. Morrison, 2010: Modeling convective-stratiform precipitation processes on a Mei-Yu front with the Weather Research and Forecasting model: Comparison with observations and sensitivity to cloud microphysics parameterization. *J. Geophys. Res.*, **115**, D18117, doi:[10.1029/2010JD013873](https://doi.org/10.1029/2010JD013873).
- Mansell, E. R., 2010: On sedimentation and advection in multimoment bulk microphysics schemes. *J. Atmos. Sci.*, **67**, 3084–3094, doi:[10.1175/2010JAS3341.1](https://doi.org/10.1175/2010JAS3341.1).
- , C. L. Ziegler, and E. C. Bruning, 2010: Simulated electrification of a small thunderstorm with two-moment bulk microphysics. *J. Atmos. Sci.*, **67**, 171–194, doi:[10.1175/2009JAS2965.1](https://doi.org/10.1175/2009JAS2965.1).
- Martin, G. M., D. W. Johnson, and A. Spice, 1994: The measurement and parameterization of effective radius of droplets in warm stratocumulus clouds. *J. Atmos. Sci.*, **51**, 1823–1842, doi:[10.1175/1520-0469\(1994\)051<1823:TMAPOE>2.0.CO;2](https://doi.org/10.1175/1520-0469(1994)051<1823:TMAPOE>2.0.CO;2).
- McCumber, M., W.-K. Tao, J. Simpson, R. Penc, and S.-T. Soong, 1991: Comparison of ice-phase microphysical parameterization schemes using numerical simulations of tropical convection. *J. Appl. Meteor.*, **30**, 985–1004, doi:[10.1175/1520-0450-30.7.985](https://doi.org/10.1175/1520-0450-30.7.985).
- Milbrandt, J. A., and M. K. Yau, 2005a: A multimoment bulk microphysics parameterization. Part I: Analysis of the role of the spectral shape parameter. *J. Atmos. Sci.*, **62**, 3051–3064, doi:[10.1175/JAS3534.1](https://doi.org/10.1175/JAS3534.1).
- , and —, 2005b: A multimoment bulk microphysics parameterization. Part II: A proposed three-moment closure and scheme description. *J. Atmos. Sci.*, **62**, 3065–3081, doi:[10.1175/JAS3535.1](https://doi.org/10.1175/JAS3535.1).
- , and R. McTaggart-Cowan, 2010: Sedimentation-induced errors in bulk microphysics schemes. *J. Atmos. Sci.*, **67**, 3931–3948, doi:[10.1175/2010JAS3541.1](https://doi.org/10.1175/2010JAS3541.1).
- , M. K. Yau, J. Mailhot, and S. Bélair, 2008: Simulation of an orographic precipitation event during IMPROVE-2. Part I: Evaluation of the triple-moment control run. *Mon. Wea. Rev.*, **136**, 3873–3893, doi:[10.1175/2008MWR2197.1](https://doi.org/10.1175/2008MWR2197.1).
- , —, —, —, and R. McTaggart-Cowan, 2010: Simulation of an orographic precipitation event during IMPROVE-2. Part II: Sensitivity to the number of moments in the bulk microphysics scheme. *Mon. Wea. Rev.*, **138**, 625–642, doi:[10.1175/2009MWR3121.1](https://doi.org/10.1175/2009MWR3121.1).
- , A. Glazer, and D. Jacob, 2012: Predicting the snow-to-liquid ratio of surface precipitation using a bulk microphysics scheme. *Mon. Wea. Rev.*, **140**, 2461–2476, doi:[10.1175/MWR-D-11-00286.1](https://doi.org/10.1175/MWR-D-11-00286.1).

- Mitchell, D. L., 1996: Use of mass- and area-dimensional power laws for determining precipitation particle terminal velocities. *J. Atmos. Sci.*, **53**, 1710–1723, doi:[10.1175/1520-0469\(1996\)053<1710:UOMAAD>2.0.CO;2](https://doi.org/10.1175/1520-0469(1996)053<1710:UOMAAD>2.0.CO;2).
- Miura, H., M. Satoh, T. Nasuno, A. T. Noda, and K. Oouchi, 2007: A Madden-Julian oscillation event realistically simulated by a global cloud-resolving model. *Science*, **318**, 1763–1765, doi:[10.1126/science.1148443](https://doi.org/10.1126/science.1148443).
- Molthan, A. L., and B. A. Colle, 2012: Comparisons of single- and double-moment microphysics schemes in the simulation of a synoptic-scale snowfall event. *Mon. Wea. Rev.*, **140**, 2982–3002, doi:[10.1175/MWR-D-11-00292.1](https://doi.org/10.1175/MWR-D-11-00292.1).
- Morrison, H., and J. A. Milbrandt, 2011: Comparison of two-moment bulk microphysics schemes in idealized supercell thunderstorm simulations. *Mon. Wea. Rev.*, **139**, 1103–1130, doi:[10.1175/2010MWR3433.1](https://doi.org/10.1175/2010MWR3433.1).
- , and —, 2014: Parameterization of cloud microphysics based on the prediction of bulk ice particle properties. Part I: Scheme description and idealized tests. *J. Atmos. Sci.*, **72**, 287–311, doi:[10.1175/JAS-D-14-0065.1](https://doi.org/10.1175/JAS-D-14-0065.1).
- , J. A. Curry, and V. I. Khorostyanov, 2005: A new double-moment microphysics parameterization for application in cloud and climate models. Part I: Description. *J. Atmos. Sci.*, **62**, 1665–1677, doi:[10.1175/JAS3446.1](https://doi.org/10.1175/JAS3446.1).
- , G. Thompson, and V. Tatarskii, 2009: Impact of cloud microphysics on the development of trailing stratiform precipitation in a simulated squall line: Comparison of one- and two-moment schemes. *Mon. Wea. Rev.*, **137**, 991–1007, doi:[10.1175/2008MWR2556.1](https://doi.org/10.1175/2008MWR2556.1).
- , S. A. Tessendorf, K. Ikeda, and G. Thompson, 2012: Sensitivity of a simulated midlatitude squall line to parameterization of raindrop breakup. *Mon. Wea. Rev.*, **140**, 2437–2460, doi:[10.1175/MWR-D-11-00283.1](https://doi.org/10.1175/MWR-D-11-00283.1).
- Muhlbauer, A., and Coauthors, 2013: Reexamination of the state of the art of cloud modeling shows real improvements. *Bull. Amer. Meteor. Soc.*, **94**, ES45–ES48, doi:[10.1175/BAMS-D-12-00188.1](https://doi.org/10.1175/BAMS-D-12-00188.1).
- Rasmussen, R., and Coauthors, 2012: How well are we measuring snow: The NOAA/FAA/NCAR winter precipitation test bed. *Bull. Amer. Meteor. Soc.*, **93**, 811–829, doi:[10.1175/BAMS-D-11-00052.1](https://doi.org/10.1175/BAMS-D-11-00052.1).
- Rotunno, R., J. B. Klemp, and M. L. Weisman, 1988: A theory for strong, long-lived squall lines. *J. Atmos. Sci.*, **45**, 463–485, doi:[10.1175/1520-0469\(1988\)045<0463:ATFSLL>2.0.CO;2](https://doi.org/10.1175/1520-0469(1988)045<0463:ATFSLL>2.0.CO;2).
- Rutledge, S. A., and P. V. Hobbs, 1983: The mesoscale and microscale structure and organization of clouds and precipitation in midlatitude cyclones. VII: A model for the “seeder-feeder” process in warm-frontal rainbands. *J. Atmos. Sci.*, **40**, 1185–1206, doi:[10.1175/1520-0469\(1983\)040<1185:TMAMSA>2.0.CO;2](https://doi.org/10.1175/1520-0469(1983)040<1185:TMAMSA>2.0.CO;2).
- , and R. A. Houze, 1987: A diagnostic modelling study of the trailing stratiform region of a midlatitude squall line. *J. Atmos. Sci.*, **44**, 2640–2656, doi:[10.1175/1520-0469\(1987\)044<2640:ADMSOT>2.0.CO;2](https://doi.org/10.1175/1520-0469(1987)044<2640:ADMSOT>2.0.CO;2).
- Skamarock, W. C., and Coauthors, 2008: A description of the Advanced Research WRF version 3. NCAR Tech. Note TN-475+STR, 113 pp. [Available online at [http://www.mmm.ucar.edu/wrf/users/docs/arw\\_v3\\_bw.pdf](http://www.mmm.ucar.edu/wrf/users/docs/arw_v3_bw.pdf).]
- Smith, P. L., 1984: Equivalent radar reflectivity factors for snow and ice particles. *J. Climate Appl. Meteor.*, **23**, 1258–1260, doi:[10.1175/1520-0450\(1984\)023<1258:ERRFFS>2.0.CO;2](https://doi.org/10.1175/1520-0450(1984)023<1258:ERRFFS>2.0.CO;2).
- Stoelinga, M. T., and Coauthors, 2003: Improvement of Microphysical Parameterization through Observational Verification Experiment. *Bull. Amer. Meteor. Soc.*, **84**, 1807–1826, doi:[10.1175/BAMS-84-12-1807](https://doi.org/10.1175/BAMS-84-12-1807).
- Tao, W.-K., and Coauthors, 2009: A multiscale modeling system developments, applications, and critical issues. *Bull. Amer. Meteor. Soc.*, **90**, 515–534, doi:[10.1175/2008BAMS2542.1](https://doi.org/10.1175/2008BAMS2542.1).
- Thompson, G., P. R. Field, R. M. Rasmussen, and W. D. Hall, 2008: Explicit forecasts of winter precipitation using an improved bulk microphysics scheme. Part II: Implementation of a new snow parameterization. *Mon. Wea. Rev.*, **136**, 5095–5115, doi:[10.1175/2008MWR2387.1](https://doi.org/10.1175/2008MWR2387.1).
- Tripoli, G. J., and W. R. Cotton, 1980: A numerical investigation of several factors contributing to the observed variable intensity of deep convection over south Florida. *J. Appl. Meteor.*, **19**, 1037–1063, doi:[10.1175/1520-0450\(1980\)019<1037:ANIOSF>2.0.CO;2](https://doi.org/10.1175/1520-0450(1980)019<1037:ANIOSF>2.0.CO;2).
- Van Weverberg, K., 2013: Impact of environmental instability on convective precipitation uncertainty associated with the nature of the rimed ice species in a bulk microphysics scheme. *Mon. Wea. Rev.*, **141**, 2841–2849, doi:[10.1175/MWR-D-13-00036.1](https://doi.org/10.1175/MWR-D-13-00036.1).
- , N. P. M. van Lipzig, and L. Delobbe, 2011: The impact of size distribution assumptions in a bulk one-moment microphysics scheme on simulated surface precipitation and storm dynamics during a low-topped supercell case in Belgium. *Mon. Wea. Rev.*, **139**, 1131–1147, doi:[10.1175/2010MWR3481.1](https://doi.org/10.1175/2010MWR3481.1).
- , A. M. Vogelmann, H. Morrison, and J. A. Milbrandt, 2012: Sensitivity of idealized squall-line simulations to the level of complexity used in two-moment bulk microphysics schemes. *Mon. Wea. Rev.*, **140**, 1883–1907, doi:[10.1175/MWR-D-11-00120.1](https://doi.org/10.1175/MWR-D-11-00120.1).
- Wacker, U., and A. Seifert, 2001: Evolution of rain water profiles resulting from pure sedimentation: Spectral vs. parameterized description. *Atmos. Res.*, **58**, 19–39, doi:[10.1016/S0169-8095\(01\)00081-3](https://doi.org/10.1016/S0169-8095(01)00081-3).
- Wang, H., W. C. Skamarock, and G. Feingold, 2009: Evaluation of scalar advection schemes in the Advanced Research WRF model using large-eddy simulations of aerosol-cloud interactions. *Mon. Wea. Rev.*, **137**, 2547–2558, doi:[10.1175/2009MWR2820.1](https://doi.org/10.1175/2009MWR2820.1).
- Weisman, M. L., and R. Rotunno, 2004: “A theory for strong long-lived squall lines” revisited. *J. Atmos. Sci.*, **61**, 361–382, doi:[10.1175/1520-0469\(2004\)061<0361:ATFSLS>2.0.CO;2](https://doi.org/10.1175/1520-0469(2004)061<0361:ATFSLS>2.0.CO;2).
- , C. A. Davis, W. Wang, and K. Manning, 2008: Experiences with 0–36-h explicit convective forecasts with the WRF-ARW model. *Wea. Forecasting*, **23**, 407–437, doi:[10.1175/2007WAF2007005.1](https://doi.org/10.1175/2007WAF2007005.1).
- Ziegler, C. L., 1985: Retrieval of thermal and microphysical variables in observed convective storms. Part I: Model development and preliminary testing. *J. Atmos. Sci.*, **42**, 1487–1509, doi:[10.1175/1520-0469\(1985\)042<1487:ROTAMV>2.0.CO;2](https://doi.org/10.1175/1520-0469(1985)042<1487:ROTAMV>2.0.CO;2).